THE JOURNAL OF PHYSICAL CHEMISTRY LETTERS
A JOURNAL OF THE AMERICAN CHEMICAL SOCIETY

pubs.acs.org/JPCL

Letter

Conical Intersection Passages of Molecules Probed by X-ray Diffraction and Stimulated Raman Spectroscopy

Yeonsig Nam,* Daniel Keefer, Artur Nenov, Irene Conti, Flavia Aleotti, Francesco Segatta, Jin Yong Lee,* Marco Garavelli, and Shaul Mukamel*

Cite This: *J. Phys. Chem. Lett.* 2021, 12, 12300−12309

Read Online

ACCESS | Metrics & More | Article Recommendations | Supporting Information

ABSTRACT: Conical intersections (CoIns) play an important role in ultrafast relaxation channels. Their monitoring remains a formidable experimental challenge. We theoretically compare the probing of the $S_2 \rightarrow S_1$ CoIn passage in 4-thiouracil by monitoring its vibronic coherences, using off-resonant X-ray-stimulated Raman spectroscopy (TRUECARS) and time-resolved X-ray diffraction (TRXD). The quantum nuclear wavepacket (WP) dynamics provides an accurate picture of the photoinduced dynamics. Upon photoexcitation, the WP oscillates among the Franck−Condon point, the S_2 minimum, and the CoIn with a 70 fs period. A vibronic coherence first emerges at 20 fs and can be observed until the S_2 state is fully depopulated. The distribution of the vibronic frequencies involved in the coherence is recorded by the TRUECARS spectrogram. The TRXD signal provides spatial images of electron densities associated with the CoIn. In combination, the two signals provide a complementary picture of the nonadiabatic passage, which helps in the study of the underlying photophysics in thiobases.

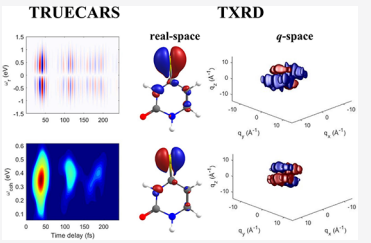

Probing conical intersection (CoIn) dynamics is important in unraveling the rates and outcomes of many photophysical and photochemical processes in molecules. At CoIns, two or more electronic surfaces become degenerate and the electronic and nuclear degrees of freedom become strongly coupled because the Born−Oppenheimer picture breaks down. This opens up ultrafast nonradiative decay channels for excited molecules. The most established techniques for observing CoIn passage are transient absorption[1−5] and photoionization spectra,[6] which give indirect signatures (state-specific information) through the change of absorption lines. These are, however, not well suited for resolving the CoIn passage due to strong contributions from populations that cover the signal from coherences. Detecting unique signatures that directly emerge from CoIn dynamics remains an open challenge, and the new protocols are in demand.

X-ray light sources, available from free-electron lasers (FELs) offer a novel window into CoIn dynamics[7,8] because of their unique temporal and spatial resolutions. Transient redistribution of ultrafast electronic coherences in attosecond Raman signals (TRUECARS) has been proposed for the direct monitoring of the CoIn passage[9] in a background-free manner. A hybrid X-ray probe field composed of a femtosecond narrowband and an attosecond broadband pulse provides phase-sensitive detection of the electronic Raman transition at the CoIn. The same information can be obtained by covariance signals with stochastic X-ray pulses.[10] TRUECARS has been employed theoretically to unveil the CoIn dynamics of uracil,[10,11] thiophenol,[12,13] and a bichromophoric heterodimer.[14]

In a different technique, time-evolving electronic charge densities at CoIn passage can be imaged with subfemtosecond resolution using ultrafast time-resolved X-ray diffraction (TRXD).[15−17] Traditionally, X-ray diffraction has been primarily used to study stationary molecular samples by elastic scattering from the ground state electron densities.[18,19] In contrast, photoexcited molecules are prepared in a time-evolving superposition of states, and inelastic scattering from different electronic states and electronic and vibrational coherences contribute to the signal.[20] Hence, TRXD can provide additional information about the CoIn passage: the momentum space image allows the reconstruction of the real-space charge density profile once the phase problem is solved.[21]

Thiouracils are nucleobases in which one or more carbonyl oxygen atoms of uracil are substituted with sulfur atoms. Thionation red-shifts the visible absorption spectra and alters their photophysics compared to that of their unsubstituted counterpart:[22] they undergo intersystem crossing (ISC) to long-lived triplet states[23,24] contrary to uracil, which undergoes ultrafast nonradiative relaxation to the ground state.[10,11,25,26] Because of their high triplet quantum yield,[24,27] thiouracils have become significantly biologically relevant, for example, as a site-specific photoprobe for photodynamic therapy[28,29] and photo-

Received: November 19, 2021
Accepted: December 17, 2021
Published: December 21, 2021

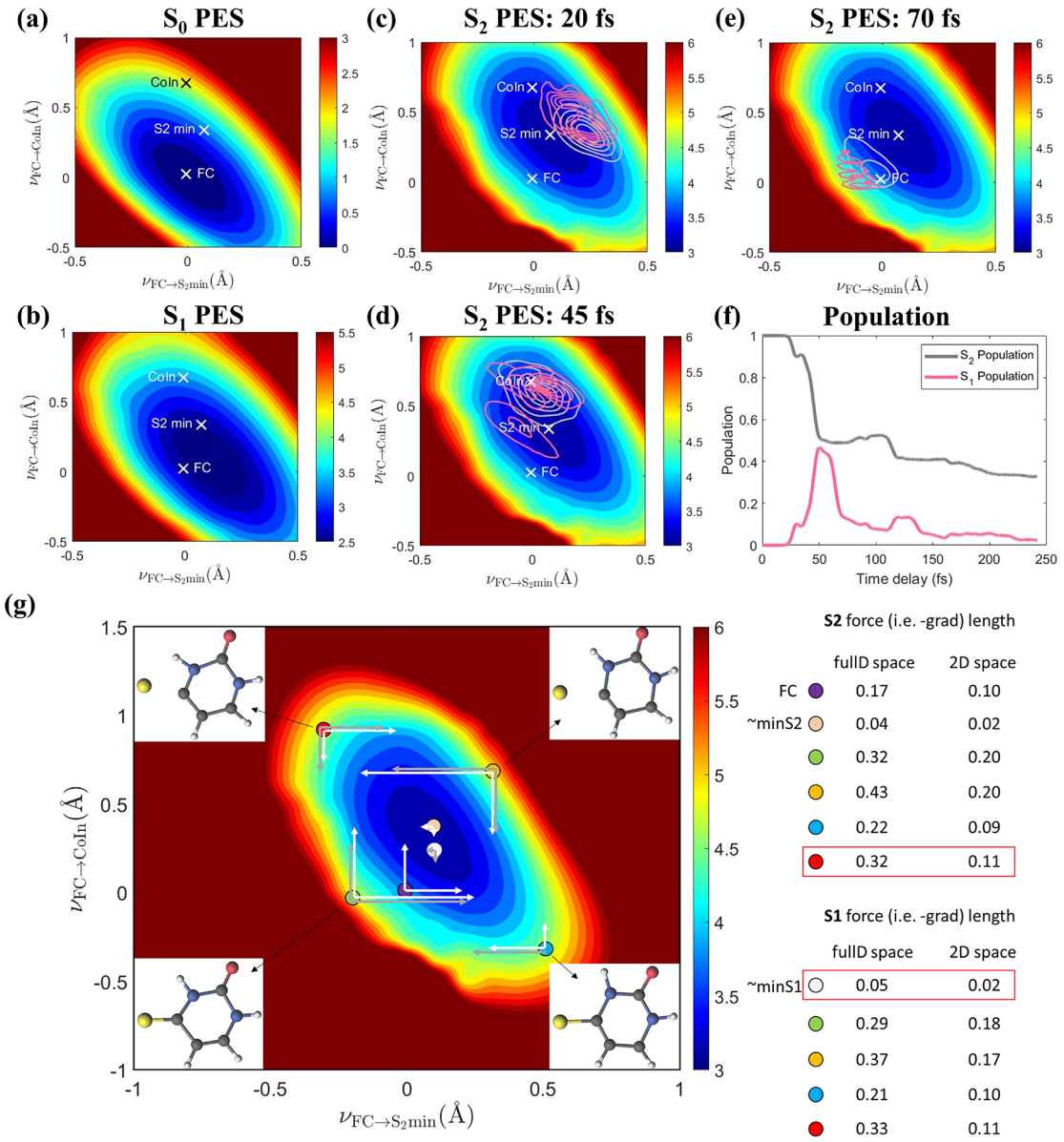

Figure 1. Potential energy surfaces and nuclear wavepacket dynamics: (a) S_0 PES, (b) S_1 PES, S_2 PES with the nuclear wavepacket at (c) 20 fs, (d) 45 fs, and (e) 70 fs, and (f) state populations: S_2 wavepacket (gray contours) and S_1 wavepacket (pink contours). The complete movie including the S_1 PES can be found in Video S2. (g) Projection of the S_2 (white arrows) and S_1 (gray arrows) gradient on the reactive coordinates. The purple, light pink, and white circles represent the locations of the FC, the S_2 min, and the S_1 min, respectively. The four molecular structures at the edges represent the geometry at the other points (red, green, blue, and orange circles). The table includes the lengths of the vectors in full-dimensional space and of the projection at the given points.

induced cross-linkers.[30,31] Moreover, they provide a good model system for unraveling how a single-atom substitution (and the location of the substitution) affects the energy relaxation pathway of DNA/RNA nucleobases. However, the nonadiabatic passage from the bright $\pi\pi^*$ state to the dark $n\pi^*$ state of 4-thiouracil (4TU) is largely unexplored, which is prototypical for all other canonical and many modified nucleo(thio)bases. It is the primary event after ultraviolet (UV) absorption, and the ongoing nuclear dynamics through the initial CoIn determines fundamental properties, like the photostability of the nucleo-(thio)bases.[25] Hence, it is a key issue to be addressed prior to unraveling the role of the $n\pi^*$ state as a doorway to the long-lived triplet manifold.

In this work, we study complementary information about the CoIn passage revealed by the TRUECARS and TRXD techniques. The former directly probes the timing and the energetic distributions of vibronic coherences, while the latter gives spatial images of the electron densities passing through the CoIns.

TRUECARS and TRXD signals are calculated on the quantum nuclear wavepacket dynamics simulation propagated by numerically integrating the time-dependent Schrödinger equation[32] in a reduced two-dimensional nuclear space spanned by $\nu_{FC\rightarrow CoIn}$, which describes the motion from the Franck–Condon (FC) to the CoIn, and $\nu_{FC\rightarrow S_2\ min}$, which represents the motion from the FC to the S_2 minimum (S_2 min). The two-dimensional potential energy surfaces and quantities required for computing the TRUECARS and TRXD signals (i.e., nonadiabatic vectors and transition densities) were computed at the state-average CASSCF level of theory followed by the

https://doi.org/10.1021/acs.jpclett.1c03814
J. Phys. Chem. Lett. 2021, 12, 12300−12309

Scheme 1. (a) Pulse Configuration, (b) Loop Diagram for TRUECARS with Randomly Oriented 4-Thiouracil,[a] and (c) Optimized Geometry for the Ground State Minimum (FC), S_2−S_1 Conical Intersection (CoIn), the S_2 Minimum (S_2 min), and the S_1 Minimum (S_1 min) and the Two Coordinate Vectors Spanning Two-Dimensional Coordinates[b]

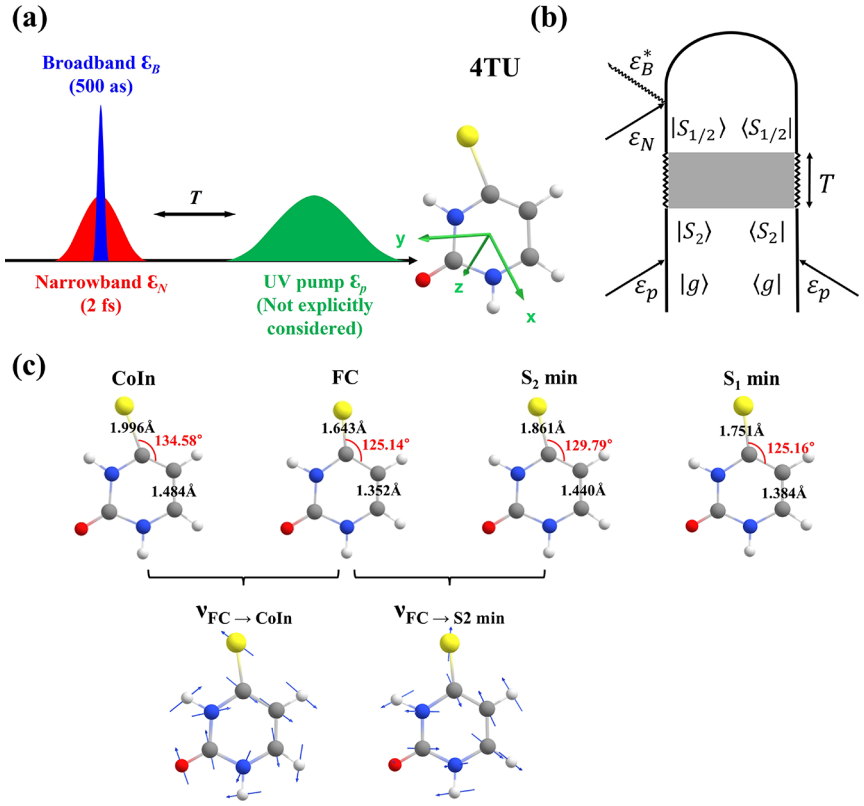

[a]The pump pulse $\mathcal{E}_p$ (not considered explicitly in the simulation) creates an electronic and nuclear population in excited state S_2. The grey area indicates a free evolution period of the molecule. At time delay T, the hybrid $\mathcal{E}_B$ (broad) and $\mathcal{E}_N$ (narrow) pulse is used to probe the dynamics. See the Supporting Information and ref 35 for loop diagram rules. [b]The C═S and C═C bond lengths are presented in black, and the ∠CCS values are presented in red.

single-state (SS) flavor second-order perturbation (CASPT2)[33] employing an active space of 12 electrons in 9 orbitals (five π orbitals, one sulfur lone pair n orbital, and three π^* orbitals) by taking the three lowest adiabatic electronic states into account [SS-CASPT2/SA-3-CASSCF(12,9)]. The ANO-L basis set[34] was used. The full protocol for quantum chemistry and nuclear wavepacket simulation is given in the Supporting Information.

We investigate the dynamics of 4TU upon impulsive photoexcitation to the S_2 ($^1\pi\pi^*$) state (the pump pulse is not explicitly included in the simulation). The potential energy surfaces of 4TU in a reduced two-dimensional (2D) nuclear space are displayed in Figure 1. The two reactive coordinates include projections on several normal modes that describe the relevant structural changes and contain all modes that are responsible for the reaction. This reflects the fact that several nuclear degrees of freedom cooperatively deform the geometry of a molecule leading to the conical intersections. Indeed, the surface hopping simulation[23] (with all nuclear degrees of freedom) reports that the $\pi\pi^*/n\pi^*$ crossing is characterized by several normal modes. Among them, C−S elongation with low frequency (457 cm^{-1}) and ring breathing modes (HC−CH stretching at 697 and 783 cm^{-1}) are dominant. Our reduced reactive coordinate vectors encompass all of these realistic normal modes to some extent; the C−S and C−C stretchings describe the relaxation to the $\pi\pi^*$ minimum and beyond toward the CoIn as demonstrated in Scheme 1c. Note, however, that this discussion is based on normal modes computed in solution, so the values should be taken as qualitative indicators.

To further demonstrate this, we display the projection of the full excited state gradients at the FC, the S_2 min, the S_1 min, and several points in the periphery of the PES onto the 2D reactive coordinates in Figure 1g. Overall, our 2D subspace quite uniformly encloses half of the full gradient except the top left corner of the PES (red circle), where the total gradient mainly describes elongation of the two C−N bonds in the ring that is not described by our 2D spaces. As for the gradient of the S_1 state, the total length and the direction of the projection show features similar to the features of those of S_2. Notably, at the point on the grid closest to the S_1 min (white circle), the S_1 state has a projected length of 0.02 out of a total length of 0.05, just as at the point on the grid closest to its respective S_2 min (pink circle, 0.02 out of 0.04). This implies that the S_1 surface is still described as well as the S_2 surface despite the S_1 min being not explicitly considered in the formulation of the reactive coordinates. We have successfully reproduced the observed time scales in photorelaxation of uracil,[11] photoisomerization of azobenzene,[36] and ring opening of cyclohexadiene[37] using this approach. The ground state is not populated because our nuclear space does not cover the $S_1 \rightarrow S_0$ CoIn(s) passage; we thus refer to CoIn as S_2/S_1 CoIn throughout unless otherwise specified.

In 4TU, the FC, the CoIn, the S_2 min, and the S_1 min structure preserve its planar structure and the differences are associated

https://doi.org/10.1021/acs.jpclett.1c03814
J. Phys. Chem. Lett. 2021, 12, 12300−12309

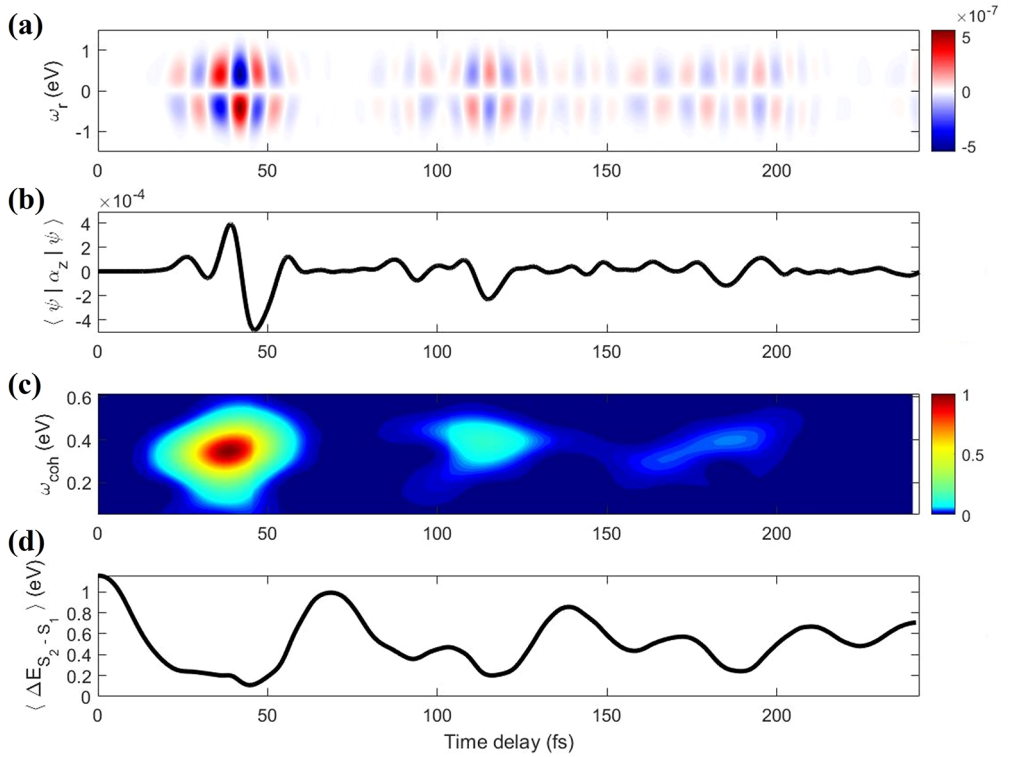

Figure 2. TRUECARS signal of 4TU. (a) Frequency-dispersed signal $S(\omega_r, T)$. (b) Expected value of the polarizablility operator α_z. (c) Frequency-resolved optical-gating spectrogram (eq 2) with signal trace $S(t)$ taken at ω_r = 0.37 eV (maximum signal intensity). (d) Expected value of the energy splitting between the S_2 and S_1 states $[\langle \Delta E_{S_2-S_1} \rangle = \langle \psi | E(S_2) - E(S_1) | \psi \rangle]$.

with the C−S bond length and the relevant ∠CCS angle, which are captured by the reactive coordinates (Scheme 1c): FC (1.643 Å, 125.14°), S_2 min (1.861 Å, 129.79°), S_1 min (1.751 Å, 125.16°), and CoIn (1.996 Å, 134.58°). This supports the idea that $\nu_{FC\rightarrow CoIn}$ and $\nu_{FC\rightarrow S_2\ min}$, which are mainly the elongation of the C−S bond, can capture the CoIn to S_1 min pathway to some extent.

The S_2 PES exhibits a single well with a barrierless pathway from the FC through the S_2 min to the CoIn, but with an energy difference of 0.3 eV between the S_2 min and the CoIn. In contrast, unmodified uracil exhibits a double well in the excited state with a small 0.5 eV barrier between the S_2 min and the CoIn peaks, and only a small part of the WP reaches the CoIn.[25] This demonstrates how even a single-atom substitution of 4TU compared to uracil can significantly influence the electronic structures and the relaxation dynamics. The nonadiabatic couplings (NACs) exhibit a characteristic change in sign at the CoIn, due to switching of the electronic character of the adiabatic states (Figure S1a).

Using the PESs and NACs, a nuclear WP was propagated by exactly solving the time-dependent Schrödinger equation for our effective Hamiltonian (the complete nuclear WP movies including the S_1 PES can be found in Video S2). Upon photoexcitation, the WP starts at the FC region and first reaches the S_2 min at 20 fs. The NAC is nonvanishing there; the S_1 electronic state is populated, and a vibronic coherence between S_2 and S_1 is created. The WP reaches the CoIn at 45 fs, where the NAC is strongest and the major CoIn relaxation takes place. The wavepacket bifurcates into S_2 and S_1 WPs with a significant overlap between them, creating a strong vibronic coherence. At 70 fs, the WPs evolve back to the FC region. Here, the presence of the $\nu_{FC\rightarrow S_2\ min}$ coordinate, despite being similar to the $\nu_{FC\rightarrow CoIn}$ coordinate, facilitates decoherence after the CoIn passage: the two WPs evolve differently, and their overlap strongly decreases over time (see Video S2): the S_1 WP moves clockwise and reaches the CoIn at ∼80 fs; the population is inversely transferred from the S_1 to the S_2 state (Figure 1f between 80 and 110 fs). The S_2 WP in contrast moves counterclockwise, and both S_1 and S_2 WPs overlap again at the CoIn at 115 fs. The WPs oscillate between the FC and the CoIn with a period of 70 fs.

In the vicinity of the S_1 min, the $T_{1/2}$ triplet state becomes nearly isoenergetic. The wavepacket will be subject to ISC, facilitated by a spin−orbit coupling. However, population of the triplet manifold out of the S_2 or S_1 state cannot be described by our two-dimensional Hamiltonian because spin−orbit crossings cannot be readily accessed by the numerical protocol and the ISC may be facilitated along other modes. Hence, the ISC dynamics is described only phenomenologically by placing the Gobbler at the S_1 min to absorb part of the wavepackets and prevent major artificial back-evolution to S_2. The artificial placement of Gobbler and its impact on the TRUECARS signal are discussed below. The S_2 population decay is fitted with an exponential function (note that the total population decreases due to the Gobbler filter), $P(t) = Ae^{-t/k} + P_0$, where A is a coefficient and P_0 is the initial population, yielding a time constant k of 56 fs. The relaxation time compares well with that from experiment (76 fs) and surface hopping simulations (67.5 fs)[23] and is faster than that computed for uracil (186 fs)[11] due to the absence of energy barriers.

The vibronic coherence between S_2 and S_1 emerging at the CoIn is probed by the TRUECARS signal using the hybrid field $\mathcal{E}_N$ (2 fs duration) and $\mathcal{E}_B$ (central frequency at 2450 eV with a 500 as duration), after the waiting time T (Scheme 1b). Note that the transition polarizability is energy-dependent on the

https://doi.org/10.1021/acs.jpclett.1c03814
J. Phys. Chem. Lett. 2021, 12, 12300−12309

central frequency of the X-ray pulse used. Other probe frequencies may be employed as long as they are off-resonant to any molecular transition. A value of 350 eV has been used for uracil.[11] A different picture of the TRUECARS signal can be observed at the different probe frequencies. The ideas for potential signal enhancement by employing a preresonant probe frequency are given in refs 10 and 14. The corresponding loop diagram is given in Scheme 1b.

The TRUECARS signal reads[9,12]

$$S(\omega_s, T) = \mathrm{Im} \int \mathrm{d}t \mathcal{E}_B^*(\omega_s)\mathcal{E}_N(t - T)\mathrm{e}^{i\omega_s(t-T)}\langle\alpha(t)\rangle \quad (1)$$

where "Im" denotes the imaginary part, $\mathcal{E}_{N/B}$ is a hybrid narrow/broadband Gaussian pulse envelope (Scheme 1b), ω_s is the carrier frequency, and T is the time delay between the pump and the probe. The S_2/S_1 transition polarizability $\alpha(t)$ is calculated from the transition charge density, $\sigma_{S_2S_1}$ (see the Supporting Information for the derivation).

The TRUECARS signals were computed in the x, y, and z polarization directions in the molecular frame (Figure S3) and then averaged to give the rotationally averaged TRUECARS signal shown in Figure 2a. This signal selectively probes the vibronic coherence in a background-free manner: it does not show up until 20 fs when the vibronic coherence first emerges and the transition polarizabilities show up (Figure 2b). At 45 fs, the TRUECARS signal reaches a maximum due to the maximal overlap of S_2/S_1 WPs and the large transition polarizabilities. After a decay period, the signal starts to reappear at 80 fs when the parts of the S_1 WP that have not been absorbed have evolved back to the CoIn. The TRUECARS signal remains visible until after 200 fs due to the delocalized nature of the S_2 WP, where its tail continues to reach the CoIn.

To verify the use of the artificial placement of Gobbler at the S_1 min and its impact on the TRUECARS signal, we performed nuclear wavepacket dynamics simulations by changing the location of the Gobbler (Figure S4). We found that placing the Gobbler closer to the CoIn (Figure S4c,d) does not affect the signals substantially. Placing Gobbler further below (Figure S4b) from the S_1 min results in larger coherences because major parts of the S_1 wavepacket are not absorbed and evolve back to the CoIn. This leads to inverse population transfer to the S_2 state and a strong signal around 200 fs. The coherence might be artificially large at the revival times (at 115 and 185 fs), which is true for any reduced coordinates. The reappearance of the observed coherence ultimately depends on the accessibility and efficiency of the ISC to the triplet state at the S_1 min, not explicitly but only phenomenologically included in our simulation. The signal around 200 fs might be stronger or weaker than predicted by our simulations. The ISC pathway does not contribute to the signal because the transition densities between the singlet and triplet states are zero. One might expect a small contribution to the signal from the internal conversion between the T_2 and T_1 states.

The TRUECARS signal exhibits temporal Stokes and anti-Stokes oscillations between positive and negative values at nonzero Raman shifts. The energetic nature of the adiabatic states in the vibronic coherence is encoded in the temporal oscillations of the frequency-dispersed signal. This is due to the dynamical phase imprinted in the coherence stemming from the energy difference between the adiabatic states.[9,11] To visualize the dynamical evolution of this frequency, a temporal trace $S(t)$ at a constant ω_r of 0.37 eV is convolved with a Gaussian gating function $E_{gate}(t)$ with a full width at half-maximum (fwhm) of 4.84 fs, affording a spectrogram resembling the frequency-resolved optical-gating (FROG) measurement:[38]

$$I_{FROG}(T, \omega_{coh}) = \left| \int_{-\infty}^{\infty} \mathrm{d}t S(t) E_{gate}(t - T)\mathrm{e}^{-i\omega_{coh}t} \right|^2 \quad (2)$$

To analyze the energetic profiles, we used Wigner[11] and FROG,[10] and both gave the spectrogram of the TRUECARS signal that contains the relevant information. The spectrogram depicted in Figure 2c exhibits strong features at 45, 115, and 185 fs. Between 100 and 200 fs, the main frequency feature first decreases to 0.4 eV and then slightly increases again but maintains an energy splitting of around 0.4 eV implying that the WP revisits the same CoIn periodically. To further extend this analysis, we have computed the expectation value of the energy splitting between S_2 and S_1, $\langle\Delta E_{S_2-S_1}\rangle = \langle\psi|E(S_2) - E(S_1)|\psi\rangle$, where $E(S_2)$ and $E(S_1)$ correspond to the potential energy surfaces of the S_2 and S_1 states, respectively (Figure 2d). The temporal profile of this expectation value coincides with that of the FROG spectrogram and with the motion of the WPs. The TRUECARS spectrogram thus provides information about the timing and the energetic profiles at the CoIn.

TRXD images electron densities evolving in the vicinity of the CoIns. This spatial information is not accessible with TRUECARS, because it requires a scattering measurement. To image the CoIn dynamics by TRXD, we have computed the transition charge densities, $\sigma_{S_2S_1}(\mathbf{q}, R)$ on a grid across the two-dimensional nuclear space. State densities $\sigma_{S_1S_1}$ and $\sigma_{S_2S_2}$ span the entire 4TU molecule and are virtually identical (Figure S5). This is due to the fact that all 66 electrons contribute to the state densities whereas only a single active electron contributes to the electronic transition. Transition charge density $\sigma_{S_2S_1}$ is mainly located around the S atom.

The TRXD signals were computed in the three-dimensional momentum space and then radially averaged to obtain the TRXD signal for a randomly oriented sample. The gas phase (single-molecule) TRXD signal of a sample with N noninteracting molecules reads[20,36,39]

$$S_1(\mathbf{q}, T) \propto N \int \mathrm{d}t |\mathcal{E}_X(t - T)|^2 \tilde{S}_1(\mathbf{q}, t) \quad (3)$$

where

$$\begin{aligned}
&\tilde{S}_1(\mathbf{q}, t) \\
&= \rho_{S_1S_1}(t)\langle\chi_{S_1}(t)|\boldsymbol{\sigma}_{S_1S_1}^{\dagger}\boldsymbol{\sigma}_{S_1S_1}|\chi_{S_1}(t)\rangle && \text{(i)} \\
&+ \rho_{S_2S_2}(t)\langle\chi_{S_2}(t)|\boldsymbol{\sigma}_{S_2S_2}^{\dagger}\boldsymbol{\sigma}_{S_2S_2}|\chi_{S_2}(t)\rangle && \text{(ii)} \\
&+ \rho_{S_1S_1}(t)\langle\chi_{S_1}(t)|\boldsymbol{\sigma}_{S_1S_2}^{\dagger}\boldsymbol{\sigma}_{S_2S_1}|\chi_{S_1}(t)\rangle && \text{(iii)} \\
&+ \rho_{S_2S_2}(t)\langle\chi_{S_2}(t)|\boldsymbol{\sigma}_{S_2S_1}^{\dagger}\boldsymbol{\sigma}_{S_1S_2}|\chi_{S_2}(t)\rangle && \text{(iv)} \\
&+ 2\mathrm{Re}[\rho_{S_2S_1}(t)\langle\chi_{S_2}(t)|\boldsymbol{\sigma}_{S_2S_2}^{\dagger}\boldsymbol{\sigma}_{S_2S_1}|\chi_{S_1}(t)\rangle \\
&+ \rho_{S_2S_1}(t)\langle\chi_{S_2}(t)|\boldsymbol{\sigma}_{S_2S_1}^{\dagger}\boldsymbol{\sigma}_{S_1S_1}|\chi_{S_1}(t)\rangle] && \text{(v)}
\end{aligned} \quad (4)$$

where each term corresponds to a specific loop diagram in Figure S6. $\rho_{S_1S_1}$ and $\rho_{S_2S_2}$ are the electronic state populations, and $\rho_{S_2S_1}$ is the corresponding coherence. The first (i) and second (ii) terms in eq 4 represent elastic scattering from the first and

https://doi.org/10.1021/acs.jpclett.1c03814
J. Phys. Chem. Lett. 2021, 12, 12300−12309

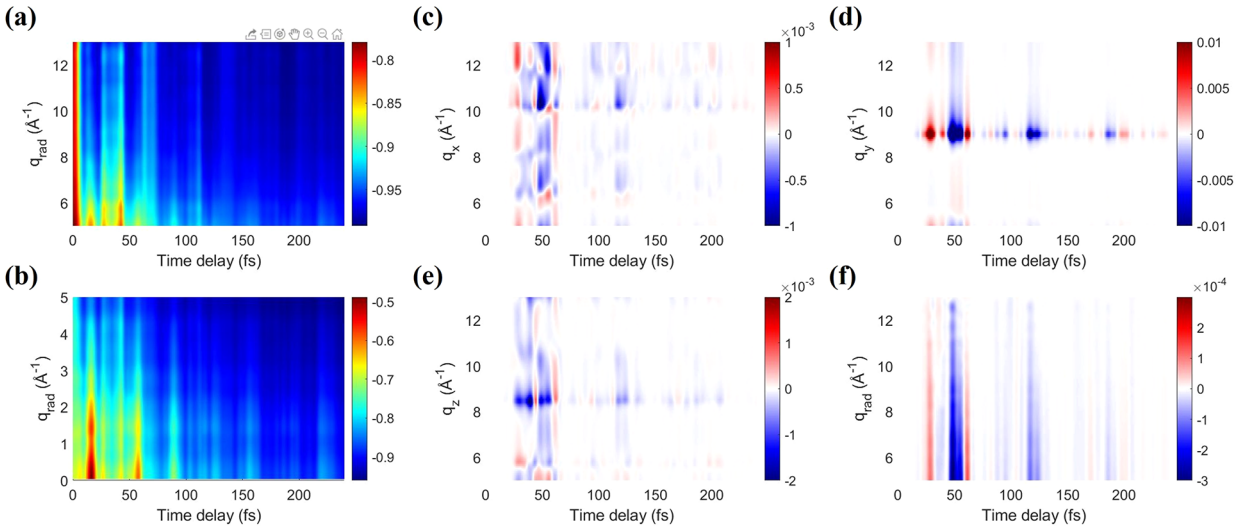

Figure 3. Normalized time-resolved diffraction signal spread along the different radial momenta ($\mathbf{q}_{rad}$) windows (a and b) and its mixed elastic/inelastic scattering contribution from the vibronic coherence (term v in eq 4) along the (c) $\mathbf{q}_x$, (d) $\mathbf{q}_y$, (e) $\mathbf{q}_z$, and (f) $\mathbf{q}_{rad}$ axes. The signals in panels c–f are represented positive/negative against −1 to emphasize their phase oscillation.

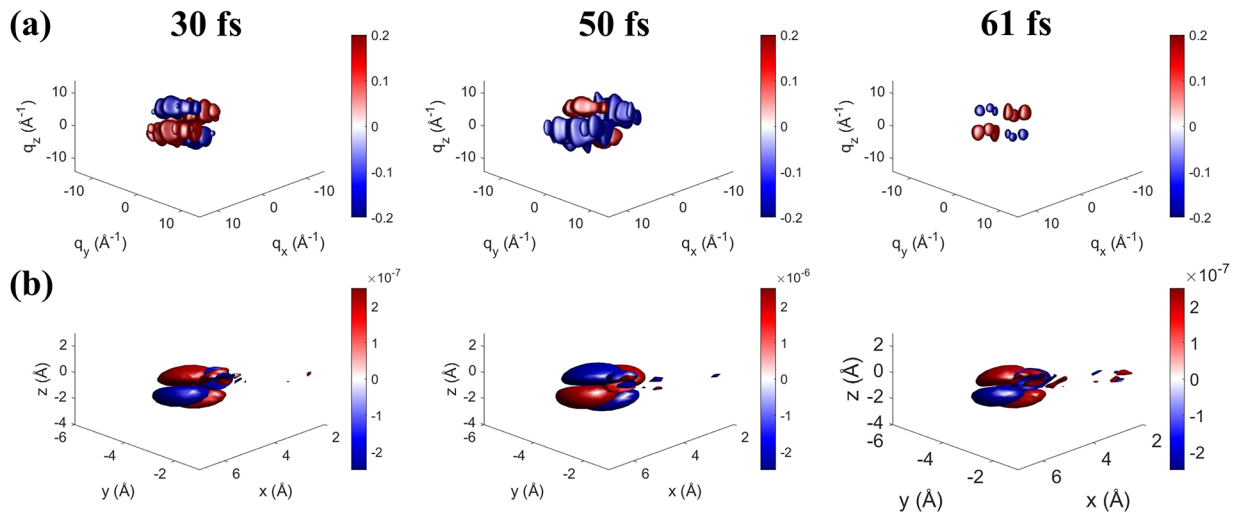

Figure 4. Three-dimensional snapshots of the contribution of the coherence to the time-resolved diffraction signal in (a) **q** space and (b) real space at 30, 50, and 61 fs.

second excited states, respectively. The third (iii) and fourth (iv) terms describe inelastic scattering from two states. The last term (v) represents the mixed elastic/inelastic scattering from vibronic coherences. The TRXD signal is presented after normalizing with the factor

$$S_1(\mathbf{q}, T) = \frac{S_1(\mathbf{q}, T) - S_1(\mathbf{q}, T < 0)}{S_1(\mathbf{q}, T < 0)} \quad (5)$$

The three-dimensional diffraction pattern and the projected diffraction signal integrating over the $\mathbf{q}_x$, $\mathbf{q}_y$, or $\mathbf{q}_z$ axis are presented in Figures S7 and S8 and discussed in the Supporting Information. The diffraction patterns show only subtle changes over time, reflecting the absence of photochemical reaction upon optical excitation but merely a photophysical relaxation between electronic states; in photorelaxation of 4TU, no major conformational changes (e.g., *cis*–*trans* isomerization or bond breaking) in the molecule occur. Below, we focus on the contribution from vibronic coherence that provides information about the CoIn.

The total, radially averaged diffraction signal is shown in panels a and b of Figure 3. The mixed (in)elastic scattering is a one-electron process; hence, the radially averaged coherence term is weak and buried under the total diffraction signal where the all-electron elastic scattering contribution is dominant. Retrieving the coherence contribution from the total signal is difficult, but it can be better observed at higher momentum transfer[36,40] because the transition density is more spread in **q** space (localized in real space) while state densities are localized in **q** space [spread across the entire molecule in real space (Figure S5)]. Also, the frequency-resolved diffraction can separate the inelastic scattering from the elastic contribution at different Raman shifts.[40]

The coherence term (v) is separately depicted in Figure 3c–f along the individual spatial directions, corresponding to a measurement with aligned molecules (Figure 3c–e), and the radially averaged axis for a randomly oriented molecule (Figure 3f). The phase oscillations between gain (red) and loss (blue) along the temporal and spatial axes are clearly seen in $\mathbf{q}_x$, $\mathbf{q}_y$, and $\mathbf{q}_z$. The temporal oscillations survive the radial averaging (Figure

https://doi.org/10.1021/acs.jpclett.1c03814
J. Phys. Chem. Lett. 2021, 12, 12300−12309

3f) and show the strongest intensities during the CoIn passage. The spatial information is somewhat concealed here because the $\mathbf{q}_y$ and $\mathbf{q}_z$ signals exhibit an opposite phase. The observed phase changes correspond to real-space phase changes of the electron density as the molecule crosses the CoIn. This is demonstrated in Figure 4, where we display the real-space densities: the phase changes at 30, 50, and 61 fs in $\mathbf{q}$ space match those found in real space. While we have access to real-space densities in the simulations, they cannot be easily extracted from experiment due to the phase problem and the radial averaging. Nevertheless, we have demonstrated that if the coherence term in $\mathbf{q}$ space is extracted, it gives direct information about the real-space phase change of the transition density.

The actual electronic coherence observed in experiments might be weaker or stronger than that predicted in our simulation. This depends on the efficiency of the $S_1 \rightarrow T_{1/2}$ ISC that we approximate by absorbing the wavepacket in the S_1 min. The observed coherence could be weaker than our simulation due to the inclusion of other nuclear degrees of freedom; however, parts of the nuclear wavepacket enter the CoIn passage, and the TRUECARS signal is qualitatively observed. Recent simulations suggest that geometric phase effects and topologies of CoIns also substantially influence the coherence strength.[41] Inclusion of an environment introduces decoherence and dephasing. This will affect the longevity but not the qualitative observations of the signals.

One could use sub-10 fs short pulses to achieve the impulsive excitation as considered in our simulation because the pulse duration is shorter than any relevant vibrational time scale. However, the realistic pump pulse may not lead to that limit. Depending on the molecular nature, a small or large population can remain in the ground state. Using realistic pump pulses in previous studies achieved, e.g., almost full population inversion in uracil[11] and 80% excitation in azobenzene.[42] In our previous work,[23,43] a sub-20 fs UV pump pulse with a range of 3.44−3.87 eV was used to excite a molecule in a ground state to the bright S_2 state. We refer to the paper that is helpful for understanding the realistic excitation process in thiobases. The nuclear WP propagating on the ground state surface would overlap with those on the S_2 or S_1 PES, yielding additional contributions to the TRUECARS signal. However, this signal would show up at the higher Raman shift (3−4 eV for 4TU) due to the finite energy gap between the S_2/S_1 and S_0 states and thus will be well separated from the S_2/S_1 conical intersection close to 0 eV.

TRXD experiments can be mearsured for weakly excited samples, extracting dynamical contributions by subtraction of the laser-off signal, the ground state background.[44] If the coherence is too weak, extracting it from the large elastic scattering background in TRXD may be too difficult. One can expect an (in)elastic scattering contribution from triplet states to the total signal, but the inelastic scattering between singlet and triplet states is prohibited and does not contribute to the total signal. The intersystem crossing occurs at a longer time scale, and the ultrafast relaxation of S_2 to S_1 is less affected. In TRUECARS, populations do not contribute to the signal. Thus, even in the weak excitation limit, no background is added that could complicate or mask the signal, and the coherences can be readily detected.

Photoionization or Auger−Meitner decay that acts as a loss channel still exists, even though it does not act as background. To maximize the number of photons that can be counted on the detector, different measures can be taken; molecules with a high transition polarizability can be chosen. This can also be enhanced by choosing a probe frequency close to a core resonance, but still far enough off-resonant such that populations do not yet contribute.[14] Finding a molecule and pulse parameters that optimize the coherences and make them equally detectable in both TRUECARS and TRXD is a challenge for future experiments. Here, we give an overview of how these signals compare in 4-thiouracil.

An established technique for accessing the conical intersections is attosecond time-resolved X-ray absorption spectroscopy (TRXAS).[1] This technique provides an accurate timing of the conical intersection by temporally resolving the absorption spectra as well as 7 fs.[45] It gives the state-specific signals through the resonant core states and vibrational coherence information. The implementation of TRXAS is less challenging and more established than TRUECARS, which is yet to be realized in practice: the broad bandwidth of the TRXAS probe pulse covers the core-excited states providing attosecond temporal resolution. One can alternatively scan a monochromatic beam to obtain the same feature. The overlapping absorption lines and the population background could complicate the selective detection of the coherences.

The proposed TRUECARS technique selectively probes the vibronic coherences with a high temporal and spectral resolution in a background-free manner; populations do not contribute to the signal. In addition to timings, the vibronic coherence structure and the transient energy splitting between the adiabatic states can be read from the spectrum. The difficulties in TREUCARS lie in the experimental implementation due to the required phase control of the hybrid broadband/narrowband pulse.

The TRXD technique requires very hard X-ray beams to realize large momentum transfers where coherences are stronger,[36] rendering the experiment very difficult. Separating out the contribution of the coherence to the total signal requires a hard X-ray above 9.5 keV FEL that limits the temporal resolution of the probe. The scattering signal is extremely weak considering that the optical excitation, and the coherence contribution is a one-electron effect on a background of the 66 electrons in 4TU. In a recent experimental work, scattering signatures with a fraction of 0.05% in the total signal for a system that has 6% of excitation fraction were measured.[46] A sophisticated control of X-ray beams and samples is required to overcome the noise.

The covariance X-ray diffraction signal, in which each individual shot of the signal is correlated with the probe pulse, has been proposed to separate coherences. This technique can offer both temporary and spectrally resolved spatial information about the evolution of the transition charge densities during the CoIn passage at a given $\mathbf{q}$. The attosecond hard X-ray FEL was theoretically suggested to generate a single-spike hard X-ray FEL pulse with an estimated fwhm pulse duration at the 200 as level at 5.6 and 9 keV.[47] Makhija et al.[48] theoretically showed that electronic anisotropies are characterized by their momenta, such as orientation and alignment; thus, electronic coherences can be separated out from population by ultrafast angle-resolved scattering measurement. These would make it feasible to implement the TRXD technique and separate the coherence contribution from stronger populations. Once all complications are solved, spatial images of the electron density around the CoIn are accessible. This spatial information is unique to scattering-based experiments and not accessible with transient absorption or stimulated Raman. We summarize the signal,

https://doi.org/10.1021/acs.jpclett.1c03814
J. Phys. Chem. Lett. 2021, 12, 12300−12309

Table 1. Comparison of the TRXAS, TRUECARS, and TRXD Techniques

technique	signal	pulse requirement	information	difficulties
TrXAS (established)	$S(\omega_s, T) = -\mathrm{Im}\ \mu_{g'f}\mu^*_{fe}\frac{\varepsilon^*_{pr}(\omega_s)\varepsilon(\omega_s)\rho_{ge'}(T)}{\omega_s - \omega_{fe'} + i\gamma_{fe'}}$	single probe pulse	precise timing state-specific information vibrational coherence	population background overlapping absorption lines
TRUECARS (proposed)	$S(\omega_s, T) = \mathrm{Im}\int \mathrm{d}t\mathcal{E}^*_B(\omega_s)\mathcal{E}_N(t-T)e^{i\omega_s(t-T)}\langle\widehat{\boldsymbol{\alpha}(t)}\rangle$	hybrid pulse (broadband/narrowband)	energetic profiles vibronic coherence structure	requires two X-ray probe pulses (phase control)
TRXD	$S(\mathbf{q}, T) = N\int \mathrm{d}t\lvert\mathcal{E}_X(t-T)\rvert^2\tilde{S}_1(\mathrm{q}, t)$	hard X-ray pulse	spatial information: electron transition densities at CoIns	extraction of coherences from the dominant population background

pulse requirement, spectroscopic information, and difficulties in the experimental implementation in Table 1.

In conclusion, we have simulated the TRUECARS and TRXD signals for the $S_2 \rightarrow S_1$ CoIn dynamics of 4TU. Quantum nuclear wavepacket dynamics performed on the effective two-dimensional PES provides an accurate picture of the relaxation dynamics and helps unveil this feature in the CoIn passage. The smaller energetic gradient between the S_2 min and the CoIn enables faster nonradiative relaxation in 4TU (67 fs) than in uracil (186 fs). The frequency-dispersed off-resonant TRUECARS technique selectively probes vibronic coherences that emerge as unique signatures during the CoIn passage. The signal remains visible until the S_2 state is fully depopulated, because the nuclear WPs on both S_2 and S_1 PES oscillate among the FC, S_2 min, and CoIn. The TRUECARS spectrograms reveal the energy splitting of adiabatic states giving detailed insight into the vibronic coherene structure. This can be employed to manipulate these coherences and thereby control CoIn passages. The off-resonant TRXD signal images the evolving charge densities during the CoIn passage in momentum space, providing a direct connection to real-space images of charge densities at CoIns. The diffraction pattern of the mixed elastic/inelastinc scattering from vibronic coherence emerges at the CoIns and shows distinct gain/loss temporal phase oscillations. This contribution is covered by the stronger elastic scattering from population states but could be singled out by looking at high scattering momentum transfer[36] or by frequency-dispersed detection.[40] Once the complications are solved, the proposed TRUECARS and TRXD can actually be performed and provide complementary information (energetic profiles and charge evolution) to decipher the CoIn relaxation pathways, which cannot be accessed in the established TRXAS technique. The detailed picture of the CoIn passages obtained by TRUECARS and TRXD would be useful for studying the underlying photophysics in thiobases.

■ ASSOCIATED CONTENT

Supporting Information

The Supporting Information is available free of charge at https://pubs.acs.org/doi/10.1021/acs.jpclett.1c03814.

(1) Simulation details, (2) derivation of the TRUECARS and TRXD signal, (3) loop diagram rule, (4) supplementary results and discussion, (5) supplementary figures, including comparison of electronic structure theory, NAC and transition polarizabilities, TRUECARS signals along the *x*, *y*, and *z* axes, TRUECARS signal upon different Gobbler, real-space electron densities, loop diagrams for X-ray scattering, two-dimensional diffraction signal along the $\mathbf{q}_{xy}$, $\mathbf{q}_{xz}$, and $\mathbf{q}_{yz}$ planes, time-resolved diffraction signal along $\mathbf{q}_x$, $\mathbf{q}_y$, $\mathbf{q}_z$, and $\mathbf{q}_{rad}$, and ratio of the coherence contribution compared to the total TRXD signal (PDF)

Nuclear wavepacket movie (Video S1) (AVI)

Three-dimensional diffraction signal movie (Video S2) (AVI)

■ AUTHOR INFORMATION

Corresponding Authors

Yeonsig Nam − *Department of Chemistry, University of California, Irvine, California 92697-2025, United States; Convergence Research Center for Energy and Environmental Sciences, Sungkyunkwan University, Suwon 16419, Korea;* orcid.org/0000-0003-0386-9118; Email: yeonsign@uci.edu

Jin Yong Lee − *Convergence Research Center for Energy and Environmental Sciences and Department of Chemistry, Sungkyunkwan University, Suwon 16419, Korea;* orcid.org/0000-0003-0360-5059; Email: jinylee@skku.edu

Shaul Mukamel − *Department of Chemistry, University of California, Irvine, California 92697-2025, United States;* orcid.org/0000-0002-6015-3135; Email: smukamel@uci.edu

Authors

Daniel Keefer − *Department of Chemistry, University of California, Irvine, California 92697-2025, United States;* orcid.org/0000-0001-5941-5567

Artur Nenov − *Dipartimento di Chimica Industriale "Toso Montanari,", Universita' degli Studi di Bologna, I-40136 Bologna, Italy;* orcid.org/0000-0003-3071-5341

Irene Conti − *Dipartimento di Chimica Industriale "Toso Montanari,", Universita' degli Studi di Bologna, I-40136 Bologna, Italy;* orcid.org/0000-0001-7982-4480

Flavia Aleotti − *Dipartimento di Chimica Industriale "Toso Montanari,", Universita' degli Studi di Bologna, I-40136 Bologna, Italy*

Francesco Segatta − *Dipartimento di Chimica Industriale "Toso Montanari,", Universita' degli Studi di Bologna, I-40136 Bologna, Italy;* orcid.org/0000-0003-4150-6676

Marco Garavelli − *Dipartimento di Chimica Industriale "Toso Montanari,", Universita' degli Studi di Bologna, I-40136 Bologna, Italy;* orcid.org/0000-0002-0796-289X

Complete contact information is available at: https://pubs.acs.org/10.1021/acs.jpclett.1c03814

https://doi.org/10.1021/acs.jpclett.1c03814
J. Phys. Chem. Lett. 2021, 12, 12300−12309

Notes

The authors declare no competing financial interest.

■ ACKNOWLEDGMENTS

This work was primarily supported by the U.S. Department of Energy, Office of Science, Office of Basic Energy Sciences, under Award DE-FG02-04ER15571 (S.M.) and Award DE-SC0019484 (M.G.). The support of the National Science Foundation through Grant CHE-1953045 is gratefully acknowledged. Y.N. acknowledges support from the Korea Initiative for fostering University of Research and Innovation Program of the National Research Foundation (NRF) funded by the Korean government (MSIT) (2020M3H1A1077095). Y.N. is grateful to Stefano M. Cavaletto for useful and interesting discussions. D.K. gratefully acknowledges support from the Alexander von Humboldt Foundation through the Feodor Lynen program.

■ REFERENCES

(1) Neville, S. P.; Chergui, M.; Stolow, A.; Schuurman, M. S. Ultrafast X-Ray Spectroscopy of Conical Intersections. *Phys. Rev. Lett.* **2018**, *120*, 243001.
(2) Timmers, H.; Li, Z.; Shivaram, N.; Santra, R.; Vendrell, O.; Sandhu, A. Coherent Electron Hole Dynamics Near a Conical Intersection. *Phys. Rev. Lett.* **2014**, *113*, 113003.
(3) Oliver, T. A. A.; Lewis, N. H. C.; Fleming, G. R. Correlating the motion of electrons and nuclei with two-dimensional electronic−vibrational spectroscopy. *Proc. Natl. Acad. Sci. U.S.A.* **2014**, *111*, 10061−10066.
(4) Raab, A.; Worth, G. A.; Meyer, H.-D.; Cederbaum, L. S. Molecular dynamics of pyrazine after excitation to the S2 electronic state using a realistic 24-mode model Hamiltonian. *J. Chem. Phys.* **1999**, *110*, 936−946.
(5) Kowalewski, M.; Mukamel, S. Stimulated Raman signals at conical intersections: Ab initio surface hopping simulation protocol with direct propagation of the nuclear wave function. *J. Chem. Phys.* **2015**, *143*, 044117.
(6) von Conta, A.; Tehlar, A.; Schletter, A.; Arasaki, Y.; Takatsuka, K.; Wörner, H. J. Conical-intersection dynamics and ground-state chemistry probed by extreme-ultraviolet time-resolved photoelectron spectroscopy. *Nat. Commun.* **2018**, *9*, 3162.
(7) Young, L.; et al. Roadmap of ultrafast x-ray atomic and molecular physics. *J. Phys. B* **2018**, *51*, 032003.
(8) Seddon, E. A.; Clarke, J. A.; Dunning, D. J.; Masciovecchio, C.; Milne, C. J.; Parmigiani, F.; Rugg, D.; Spence, J. C. H.; Thompson, N. R.; Ueda, K.; Vinko, S. M.; Wark, J. S.; Wurth, W. Short-wavelength free-electron laser sources and science: a review. *Rep. Prog. Phys.* **2017**, *80*, 115901.
(9) Kowalewski, M.; Bennett, K.; Dorfman, K. E.; Mukamel, S. Catching Conical Intersections in the Act: Monitoring Transient Electronic Coherences by Attosecond Stimulated X-Ray Raman Signals. *Phys. Rev. Lett.* **2015**, *115*, 193003.
(10) Cavaletto, S. M.; Keefer, D.; Mukamel, S. High Temporal and Spectral Resolution of Stimulated X-Ray Raman Signals with Stochastic Free-Electron-Laser Pulses. *Phys. Rev. X* **2021**, *11*, 011029.
(11) Keefer, D.; Schnappinger, T.; de Vivie-Riedle, R.; Mukamel, S. Visualizing conical intersection passages via vibronic coherence maps generated by stimulated ultrafast X-ray Raman signals. *Proc. Natl. Acad. Sci. U.S.A.* **2020**, *117*, 24069−24075.
(12) Cho, D.; Mukamel, S. Stimulated X-ray Raman Imaging of Conical Intersections. *J. Phys. Chem. Lett.* **2020**, *11*, 33−39.
(13) Cho, D.; Rouxel, J. R.; Mukamel, S. Stimulated X-ray Resonant Raman Spectroscopy of Conical Intersections in Thiophenol. *J. Phys. Chem. Lett.* **2020**, *11*, 4292−4297.
(14) Keefer, D.; Freixas, V. M.; Song, H.; Tretiak, S.; Fernandez-Alberti, S.; Mukamel, S. Monitoring molecular vibronic coherences in a bichromophoric molecule by ultrafast X-ray spectroscopy. *Chem. Sci.* **2021**, *12*, 5286−5294.
(15) Vrakking, M. J. J.; Elsaesser, T. X-rays inspire electron movies. *Nat. Photonics* **2012**, *6*, 645−647.
(16) Glownia, J. M.; Natan, A.; Cryan, J. P.; Hartsock, R.; Kozina, M.; Minitti, M. P.; Nelson, S.; Robinson, J.; Sato, T.; van Driel, T.; Welch, G.; Weninger, C.; Zhu, D.; Bucksbaum, P. H. Self-Referenced Coherent Diffraction X-Ray Movie of Ångstrom- and Femtosecond-Scale Atomic Motion. *Phys. Rev. Lett.* **2016**, *117*, 153003.
(17) Miller, R. J. D.; Paré-Labrosse, O.; Sarracini, A.; Besaw, J. E. Three-dimensional view of ultrafast dynamics in photoexcited bacteriorhodopsin in the multiphoton regime and biological relevance. *Nat. Commun.* **2020**, *11*, 1240.
(18) Fromme, P.; Spence, J. C. Femtosecond nanocrystallography using X-ray lasers for membrane protein structure determination. *Curr. Opin. Struct. Biol.* **2011**, *21*, 509−516.
(19) Küpper, J.; et al. X-Ray Diffraction from Isolated and Strongly Aligned Gas-Phase Molecules with a Free-Electron Laser. *Phys. Rev. Lett.* **2014**, *112*, 083002.
(20) Bennett, K.; Kowalewski, M.; Rouxel, J. R.; Mukamel, S. Monitoring molecular nonadiabatic dynamics with femtosecond X-ray diffraction. *Proc. Natl. Acad. Sci. U.S.A.* **2018**, *115*, 6538−6547.
(21) Son, S.-K.; Chapman, H. N.; Santra, R. Multiwavelength Anomalous Diffraction at High X-Ray Intensity. *Phys. Rev. Lett.* **2011**, *107*, 218102.
(22) Nenov, A.; Conti, I.; Borrego-Varillas, R.; Cerullo, G.; Garavelli, M. Linear absorption spectra of solvated thiouracils resolved at the hybrid RASPT2/MM level. *Chem. Phys.* **2018**, *515*, 643−653.
(23) Borrego-Varillas, R.; Teles-Ferreira, D. C.; Nenov, A.; Conti, I.; Ganzer, L.; Manzoni, C.; Garavelli, M.; Maria de Paula, A.; Cerullo, G. Observation of the Sub-100 fs Population of a Dark State in a Thiobase Mediating Intersystem Crossing. *J. Am. Chem. Soc.* **2018**, *140*, 16087−16093.
(24) Pollum, M.; Jockusch, S.; Crespo-Hernández, C. E. Increase in the photoreactivity of uracil derivatives by doubling thionation. *Phys. Chem. Chem. Phys.* **2015**, *17*, 27851−27861.
(25) Keefer, D.; Thallmair, S.; Matsika, S.; de Vivie-Riedle, R. Controlling Photorelaxation in Uracil with Shaped Laser Pulses: A Theoretical Assessment. *J. Am. Chem. Soc.* **2017**, *139*, 5061−5066.
(26) Reiter, S.; Keefer, D.; de Vivie-Riedle, R. RNA Environment Is Responsible for Decreased Photostability of Uracil. *J. Am. Chem. Soc.* **2018**, *140*, 8714−8720.
(27) Pollum, M.; Martínez-Fernández, L.; Crespo-Hernández, C. E. In *Photoinduced Phenomena in Nucleic Acids I: Nucleobases in the Gas Phase and in Solvents*; Barbatti, M., Borin, A. C., Ullrich, S., Eds.; Springer International Publishing: Cham, Switzerland, 2015; pp 245−327.
(28) Pollum, M.; Lam, M.; Jockusch, S.; Crespo-Hernández, C. E. Dithionated Nucleobases as Effective Photodynamic Agents against Human Epidermoid Carcinoma Cells. *ChemMedChem.* **2018**, *13*, 1044−1050.
(29) Reichardt, C.; Guo, C.; Crespo-Hernández, C. E. Excited-State Dynamics in 6-Thioguanosine from the Femtosecond to Microsecond Time Scale. *J. Phys. Chem. B* **2011**, *115*, 3263−3270.
(30) Favre, A.; Moreno, G.; Blondel, M.; Kliber, J.; Vinzens, F.; Salet, C. 4-thiouridine photosensitized RNA-protein crosslinking in mammalian cells. *Biochem. Biophys. Res. Commun.* **1986**, *141*, 847−854.
(31) Meisenheimer, K. M.; Koch, T. H. Photocross-Linking of Nucleic Acids to Associated Proteins. *Crit. Rev. Biochem. Mol. Biol.* **1997**, *32*, 101−140.
(32) Tal-Ezer, H.; Kosloff, R. An accurate and efficient scheme for propagating the time dependent Schrödinger equation. *J. Chem. Phys.* **1984**, *81*, 3967−3971.
(33) Finley, J.; Malmqvist, P.-Å.; Roos, B. O.; Serrano-Andrés, L. The multi-state CASPT2 method. *Chem. Phys. Lett.* **1998**, *288*, 299−306.
(34) Widmark, P.-O.; Malmqvist, P.-Å.; Roos, B. O. Density matrix averaged atomic natural orbital (ANO) basis sets for correlated molecular wave functions. *Theor. Chim. Acta* **1990**, *77*, 291−306.
(35) Mukamel, S.; Rahav, S. In *Advances in Atomic, Molecular, and Optical Physics*; Arimondo, E., Berman, P., Lin, C., Eds.; Advances in Atomic, Molecular, and Optical Physics; Academic Press, 2010; Vol. *59*, pp 223−263.

https://doi.org/10.1021/acs.jpclett.1c03814
J. Phys. Chem. Lett. 2021, 12, 12300−12309

(36) Keefer, D.; Aleotti, F.; Rouxel, J. R.; Segatta, F.; Gu, B.; Nenov, A.; Garavelli, M.; Mukamel, S. Imaging conical intersection dynamics during azobenzene photoisomerization by ultrafast X-ray diffraction. *Proc. Natl. Acad. Sci. U.S.A.* **2021**, *118*, e2022037118.
(37) Hofmann, A.; de Vivie-Riedle, R. Quantum dynamics of photoexcited cyclohexadiene introducing reactive coordinates. *J. Chem. Phys.* **2000**, *112*, 5054−5059.
(38) Trebino, R.; DeLong, K. W.; Fittinghoff, D. N.; Sweetser, J. N.; Krumbügel, M. A.; Richman, B. A.; Kane, D. J. Measuring ultrashort laser pulses in the time-frequency domain using frequency-resolved optical gating. *Rev. Sci. Instrum.* **1997**, *68*, 3277−3295.
(39) Rouxel, J. R.; Keefer, D.; Mukamel, S. Signatures of electronic and nuclear coherences in ultrafast molecular x-ray and electron diffraction. *Struct. Dyn.* **2021**, *8*, 014101.
(40) Cavaletto, S. M.; Keefer, D.; Rouxel, J. R.; Aleotti, F.; Segatta, F.; Garavelli, M.; Mukamel, S. Unveiling the spatial distribution of molecular coherences at conical intersections by covariance X-ray diffraction signals. *Proc. Natl. Acad. Sci. U.S.A.* **2021**, *118*, e2105046118.
(41) Neville, S. P.; Stolow, A.; Schuurman, M. S. The role of geometric phase in the formation of electronic coherences at conical intersections. *arXiv* **2020**, 2011.06728.
(42) Keefer, D.; Rouxel, J. R.; Aleotti, F.; Segatta, F.; Garavelli, M.; Mukamel, S. Diffractive Imaging of Conical Intersections Amplified by Resonant Infrared Fields. *J. Am. Chem. Soc.* **2021**, *143*, 13806−13815.
(43) Borrego-Varillas, R.; Ganzer, L.; Cerullo, G.; Manzoni, C. Ultraviolet Transient Absorption Spectrometer with Sub-20-fs Time Resolution. *Appl. Sci.* **2018**, *8*, 989.
(44) Yong, H.; et al. Observation of the molecular response to light upon photoexcitation. *Nat. Commun.* **2020**, *11*, 2157.
(45) Zinchenko, K. S.; Ardana-Lamas, F.; Seidu, I.; Neville, S. P.; Van Der Veen, J.; Lanfaloni, V. U.; Schuurman, M. S.; Wörner, H. J. Sub-7-fs conical-intersection dynamics probed at the carbon K-edge. *Science* **2021**, *371*, 489.
(46) Stankus, B.; et al. Ultrafast X-ray scattering reveals vibrational coherence following Rydberg excitation. *Nat. Chem.* **2019**, *11*, 716−721.
(47) Huang, S.; Ding, Y.; Feng, Y.; Hemsing, E.; Huang, Z.; Krzywinski, J.; Lutman, A. A.; Marinelli, A.; Maxwell, T. J.; Zhu, D. Generating Single-Spike Hard X-Ray Pulses with Nonlinear Bunch Compression in Free-Electron Lasers. *Phys. Rev. Lett.* **2017**, *119*, 154801.
(48) Makhija, V.; Veyrinas, K.; Boguslavskiy, A. E.; Forbes, R.; Wilkinson, I.; Lausten, R.; Neville, S. P.; Pratt, S. T.; Schuurman, M. S.; Stolow, A. Ultrafast molecular frame electronic coherences from lab frame scattering anisotropies. *J. Phys. B: At. Mol. Opt. Phys.* **2020**, *53*, 114001.

https://doi.org/10.1021/acs.jpclett.1c03814
J. Phys. Chem. Lett. 2021, 12, 12300−12309

-Supporting Information-
Conical Intersection Passages of Molecules Probed by X-ray Diffraction and Stimulated Raman Spectroscopy

Yeonsig Nam[*,a,b], Daniel Keefer[a], Artur Nenov[c], Irene Conti[c], Flavia Aleotti[c], Francesco Segatta[c], Jin Yong Lee[*,b,d], Marco Garavelli[c], and Shaul Mukamel[*,a]

[a]Department of Chemistry, University of California, Irvine, California 92697-2025, United States
[b]Convergence Research Center for Energy and Environmental Sciences, Sungkyunkwan University, Suwon 16419, Korea
[c]Dipartimento di Chimica Industriale "Toso Montanari," Universita' degli Studi di Bologna, I-40136 Bologna, Italy

[d]Department of Chemistry, Sungkyunkwan University, Suwon 16419, Korea
[*]yeonsign@uci.edu, jinylee@skku.edu, smukamel@uci.edu

December 14, 2021

Contents

1 Simulation Details

1.1 Quantum Chemistry

The potential energy surfaces (PESs) for the adiabatic states were calculated using OpenMOLCAS program [1] at the state-average CASSCF level of theory followed by the second order perturbation (CASPT2) [2] employing an active space of 12 electrons in 9 orbitals (5 π, one sulfur lone pair n, and 3 π^* orbitals) by taking three lowest adiabatic electronic states into account (SS-CASPT2/SA-3-CASSCF(12,9)). The CASPT2 calculations were performed with the single state (SS) flavor, using an imaginary shift of 0.2 and setting the IPEA shift to 0.0. The ANO-L basis set [3] was used, with contractions 5s4p2d1f on sulfur, 4s3p2d1f on carbon, oxygen, nitrogen atoms, and 3s2p1d on hydrogen atoms.

The geometry of the Franck-Condon point (FC) is optimized at the MP2 level, whereas the geometries of the S_1 minimum (S_1 min), S_2 minimum (S_2min), and the S_2/S_1 conical intersection (CoIn) are optimized at SS-CASPT2/SA-3-CASSCF(12,9) level with the COMBRAMM [4] interface with OpenMolcas (Figure S1). When the ground state is energetically separated from the excited states, its wavefunction is dominated by the closed shell HF configuration, as the case of 4TU, the use of MP2 instead of CASPT2 is fully justified. The use of MP2 for the ground state, and CASSCF/CASPT2 for excited states is a common practice [5, 6, 7]. A comparison of the electronic structure at the critical points (FC, S_2 min, S_1 min, and S_2/S_1 CoIn) at various flavors of the CASPT2 protocol, single state (SS-PT2), extended multi state (XMS-PT2) and multi state (MS), is provided in the Table S1 and the discussed in the "Results and Discussion" section. We opt for SS-CASPT2 for its smaller electronic energy splitting between the $\pi\pi^*$ and $n\pi^*$ states.

The FC, the S_2min, and the S_2/S_1 CoIn structures were then used to construct two nuclear degrees of freedom for our effective Hamiltonian [8, 9] (Scheme 1c). The first coordinate $\boldsymbol{\nu}_{\mathrm{FC}\to\mathrm{CoIn}}$ is the normalized displacement vector that points from the FC to the CoIn. $\boldsymbol{\nu}_{\mathrm{FC}\to S_2\mathrm{min}}$ is the displacement vector from the FC to the local S_2 min which is then orthonormalized with respect to $\boldsymbol{\nu}_{\mathrm{FC}\to\mathrm{CoIn}}$. Nonadiabatic couplings (NACs) were computed analytically at the SA-3-CASSCF(12,9) level, and then were corrected (i.e. uniformly rescaled) by a scaling factor equal to the ratio between the CASSCF and the CASPT2 energy difference between S_2 and S_1 states.

The state and transition densities $\sigma(\boldsymbol{q},\boldsymbol{R})$ were evaluated in 0.1 $\mathring{A}$ increments for both $\boldsymbol{\nu}_{\mathrm{FC}\to\mathrm{CoIn}}$ and $\boldsymbol{\nu}_{\mathrm{FC}\to S_2\mathrm{min}}$ coordinates, giving $16\times 11 = 176$ total of the grid points. They were evaluated from the state specific charge density matrices P^{ij}_{rs} (calculated using the CASSCF wavefunctions) according to

$$\sigma_{ij}(\boldsymbol{q},\boldsymbol{R}) = \int d\boldsymbol{r} e^{-i\boldsymbol{q}\boldsymbol{r}} \sum_{rs} P^{ij}_{rs}(\boldsymbol{R})\phi^*_r(\boldsymbol{r},\boldsymbol{R})\phi_r(\boldsymbol{r},\boldsymbol{R}), \tag{S1}$$

using the basis set of atomic orbitals $\phi_r(\boldsymbol{r})$. There are a total of 300 $\phi_r(\boldsymbol{r})$ for 4TU (30 for each nitrogen, carbon, and oxygen, 34 for sulfur, and 14 for each hydrogen). All 66 electrons of 4TU contribute to the diagonal state densities, σ_{ii}, while the transition density σ_{ij} consist of one electron located in the sulfur lone pairs.

1.2 Wavepacket Simulations

The PESs and all molecular quantities are discretized on a spatial grid of 128x128 grid points in $\boldsymbol{\nu}_{\mathrm{FC}\to\mathrm{CoIn}}$ and $\boldsymbol{\nu}_{\mathrm{FC}\to S_2\mathrm{min}}$ by inter/extra-polation. Nuclear wavepacket simulations are then per-

formed by numerically integrating the time-dependent Schrodinger equation [10]:

$$i\hbar\frac{\partial}{\partial t}\psi = \boldsymbol{H}\psi = \left[\boldsymbol{T}_{\nu} + \boldsymbol{V}\right]\psi, \tag{S2}$$

with the kinetic energy operator $\boldsymbol{T}_{\nu}$ of the nuclei in internal coordinates $\boldsymbol{\nu}$, the potential energy operator $\boldsymbol{V}$. The time-dependent Schrodinger equation is solved exactly: the quantum nature of the nuclear wavepacket, e.g., geometric phase, and the bifurcation process at CoIn are fully captured[9]. It is ensured by tracking the phase of the electronic states during calculation of the non-adiabatic couplings, leading to their peaked nature and the phase jumps across the CoIn. This contrasts to more approximate approaches e.g., the multi-configurational time-dependent Hartree (MCTDH)[11] where the wavepacket is expressed by a sum of products of individual "configurations", or ab-initio multiple spawning (AIMS)[12] that propagates Gaussian functions and spawns new ones at excited state crossings. Treating the nuclear motions classically, e.g., surface hopping or Ehrenfest dynamics, propagates nuclear wavefunction by all nuclear degrees of freedom, but quantum natures are lost.

We expand the total time-dependent molecular wavefunction $\psi(\boldsymbol{r}, \boldsymbol{R}, t)$ in the adiabatic basis

$$\psi(\boldsymbol{r}, \boldsymbol{R}, t) = \sum_i c_i(t)\chi(\boldsymbol{R}, t)\phi(\boldsymbol{r}, \boldsymbol{R}) \tag{S3}$$

where $\chi(\boldsymbol{R}, t)$ is the normalized nuclear wavepacket in the adiabatic electronic state $\phi(\boldsymbol{r}, \boldsymbol{R})$, and c_i is the coefficient (amplitude) of adiabatic states. The starting wavepacket is obtained by impulsive excitation of the ground state vibrational wavefunction from S_0 to S_2. The Chebychev propagation scheme [10] with a time step of 0.048 fs is employed to propagate this wavepacket until the final time of 242 fs. To set up the kinetic energy operator, the G-matrix formalism [13]was employed as

$$\boldsymbol{T}_{\boldsymbol{\nu}} \simeq -\frac{\hbar^2}{2m}\sum_{r=1}^{M}\sum_{s=1}^{M}\frac{\partial}{\partial \boldsymbol{\nu}_r}\left[\boldsymbol{G}_{rs}\frac{\partial}{\partial \boldsymbol{\nu}_s}\right] \tag{S4}$$

with the G-matrix computed via its inverse elements

$$(G^{-1})_{rs} = \sum_{i=1}^{3N} m_i \frac{\partial \boldsymbol{x}_i}{\partial \boldsymbol{\nu}_r}\frac{\partial \boldsymbol{x}_i}{\partial \boldsymbol{\nu}_s} \tag{S5}$$

In the case of the 4TU coordinates, the G-matrix elements are $G_{\nu_r\nu_r} = 0.00007234 a.u.$, $G_{\nu_s\nu_s} = 0.00009237 a.u.$, and the kinetic coupling $G_{\nu_r\nu_s} = -0.00002765 a.u.$.

Our effective Hamiltonian is designed for describing the transition from the S_2 to the S_1 state and it may not be accurate to describe the WP propagation in the S_1 PES since other nuclear degrees of freedom not captured by our Hamiltonian become relevant. For example, $S_2 \rightarrow T_2 \rightarrow T_1$ or $S_2 \rightarrow S_1 \rightarrow T_1$ competitive pathways exist in 4TU [5], where the latter being more efficient (ca. 75%)[14]. The $S_1 \rightarrow T_1$ pathway occurs on a longer timescale of ca. 225fs in solution[5]. We expect a similar timescale although our system is in gas-phase. In the vicinity of the S_1 min, the $T_{1/2}$ state becomes nearly isoenergetic. The wavepacket will be subject to intersystem crossing (ISC), facilitated by a spin-orbit coupling. However, population of the triplet manifold out of the S_2 or S_1 state cannot be described by our two-dimensional Hamiltonian since spin-orbit crossings are not readily accessible by the numerical protocol and the ISC may be facilitated along other

modes. Hence, the ISC dynamics is described only phenomenologically by placing the Gobbler at the S_1 min to absorb the part of the wavepackets and prevent major artificial back-evolution to S_2. The filter was of right-pass type and placed at $\nu_{\mathrm{FC}\rightarrow\mathrm{CoIn}} = -0.1 a.u.$ with an order of 100.

2 Signal Derivation

2.1 Off-Resonant TRUECARS Signal

The TRUECARS technique involves stimulated X-ray Raman process: A narrowband $\boldsymbol{\mathcal{E}}_N$ pulse excites the system, and broadband $\boldsymbol{\mathcal{E}}_B$ pulse stimulates the emission of the photon. The associated loop diagram is shown in Scheme 1b in the main manuscript. The off-resonant stimulated Raman process, in the rotating wave approximation, is described by the following multipolar light-matter interaction Hamiltonian [15]

$$\boldsymbol{H}_{\mathrm{int}} = -\boldsymbol{\alpha}(\boldsymbol{\mathcal{E}}_B^{\dagger}\boldsymbol{\mathcal{E}}_N + \boldsymbol{\mathcal{E}}_N^{\dagger}\boldsymbol{\mathcal{E}}_B) \tag{S6}$$

where $\boldsymbol{\alpha}$ is the electronic polarizability operator, and $\boldsymbol{\mathcal{E}}_{N/B}$ are narrowband/broadband electric-field operator, respectively:

$$\boldsymbol{\mathcal{E}}_{B/N} = i\sum_s \sqrt{\frac{2\pi\omega_s}{V}}\boldsymbol{\epsilon}_s \boldsymbol{a}_s e^{i\boldsymbol{k}_s \boldsymbol{r}} \tag{S7}$$

V is the quantization volume, and $\boldsymbol{a}_s^{(\dagger)}$ are the annihilation (creation) operators of a photon with frequency ω_s, respectively. The Raman interaction from the broadband $\boldsymbol{\mathcal{E}}_B^{\dagger}\boldsymbol{\mathcal{E}}_B$ or the narrowband $\boldsymbol{\mathcal{E}}_N^{\dagger}\boldsymbol{\mathcal{E}}_N$ also contribute to the signal, but is neglected in our model Hamiltonian. The narrow/broadband single probe pulse do not provide a temporal/spectral resolution of the hybrid scheme. In the presence of pump and probe pulses, one can assume that the pump pulse is more intense than the probe pulse. In this case, the $\boldsymbol{\mathcal{E}}_N^{\dagger}\boldsymbol{\mathcal{E}}_B$ or $\boldsymbol{\mathcal{E}}_B^{\dagger}\boldsymbol{\mathcal{E}}_N$ interaction will be stronger than the $\boldsymbol{\mathcal{E}}_N^{\dagger}\boldsymbol{\mathcal{E}}_N$ or $\boldsymbol{\mathcal{E}}_B^{\dagger}\boldsymbol{\mathcal{E}}_B$ and one can neglect this weak latter contributions. The TRUECARS signal is defined in terms of the frequency-resolved probe pulse intensity after passing through the sample. Hence, it is given by the time-integrated rate of change of the number of photons of frequency ω_s in the $\boldsymbol{\mathcal{E}}_B$ pulse

$$S(\boldsymbol{k}_s) = \int dt \left\langle \frac{d}{dt}\boldsymbol{N}_s^B \right\rangle \tag{S8}$$

where $\boldsymbol{N}_s^B = \boldsymbol{a}_s^{\dagger}\boldsymbol{a}_s$ is the number operator of a photon with the detected signal frequency ω_s, stimulately emitted by $\boldsymbol{\mathcal{E}}_B$ pulse. The signal is calculated by propagating Heisenberg equations of motion for photon number operator, via the commutator $[\boldsymbol{H}_{\mathrm{int}}, \boldsymbol{N}_s^B]$. We use classical electric fields,

$$\boldsymbol{\mathcal{E}}_N = \mathcal{E}_N(t-T)e^{-i\omega_s(t-T)}e^{i\phi_N} \qquad\qquad \boldsymbol{\mathcal{E}}_B = \mathcal{E}_B(\omega_s)e^{i\phi_B} \tag{S9}$$

where $\mathcal{E}_{B/N}$ are envelope function with carrier frequency ω_s, centered at the time delay T. We match the phase of narrowband and broadband pulse so that $(\phi_B = \phi_N)$, then the off-resonant TRUECARS signal becomes

$$S(\omega_s, T) = 2\mathrm{Im}\int dt e^{-i\omega_s(t-T)}\mathcal{E}_B(\omega_s)^*\mathcal{E}_N(t-T)\langle\boldsymbol{\alpha}(t)\rangle \tag{S10}$$

where 'Im' and 'Re' refer to imaginary and real part of the term. We expand the total time-dependent molecular wavefunction $\psi(\boldsymbol{r}, \boldsymbol{R}, t)$ in the adiabatic basis

$$\psi(\boldsymbol{r}, \boldsymbol{R}, t) = \sum_i c_i(t)\chi(\boldsymbol{R}, t)\phi(\boldsymbol{r}, \boldsymbol{R}) \tag{S11}$$

where $\chi(\boldsymbol{R}, t)$ is the normalized nuclear wavepacket in the adiabatic electronic state $\phi(\boldsymbol{r}, \boldsymbol{R})$, and c_i is the coefficient (amplitude) of adiabatic states. We rewrite the expectation value $\langle ... \rangle$ in Eq. S10 explicitly in terms of the total (nuclear and electronic) wavefunction $|\psi(t)\rangle$

$$S(\omega_s, T) = 2\mathrm{Im} \int dt e^{i\omega(t-T)} \mathcal{E}_B(\omega_s)^* \mathcal{E}_N(t-T) \langle \psi(t) | \boldsymbol{\alpha} | \psi(t) \rangle \tag{S12}$$

The minimal-coupling Hamiltonian [16] provides the complete formalism to describe the interaction between light and matter by avoiding the multipolar expansion. The effective light-matter interaction Hamiltonian in Eq. S6 and the polarizability operator therein can be expressed in terms of molecular charge- and current density operators. By discarding the resonant interaction term $\boldsymbol{j} \cdot \boldsymbol{A}$ [17],

$$\boldsymbol{H}_{\mathrm{int}} = \frac{1}{2} \int d\boldsymbol{r} \boldsymbol{\sigma}(\boldsymbol{r}) \left(\boldsymbol{\mathcal{E}}_B^\dagger(\boldsymbol{r}) \boldsymbol{\mathcal{E}}_N(\boldsymbol{r}) + \boldsymbol{\mathcal{E}}_N^\dagger(\boldsymbol{r}) \boldsymbol{\mathcal{E}}_B(\boldsymbol{r}) \right) \tag{S13}$$

$$\boldsymbol{\alpha}_{\mathrm{eff}}(t) = \int d\boldsymbol{r} \int d\boldsymbol{r}' \boldsymbol{\sigma}(\boldsymbol{r}, t) e^{i\boldsymbol{k}(\boldsymbol{r}-\boldsymbol{r}')} \tag{S14}$$

where $\boldsymbol{\sigma}(\boldsymbol{r})$ term is the charge-density operator. Integrating over r and r' gives,

$$\langle \boldsymbol{\sigma}(\boldsymbol{q}, t) \rangle = \int d\boldsymbol{r} e^{-i\boldsymbol{q}\boldsymbol{r}} \langle \boldsymbol{\sigma}(\boldsymbol{r}, t) \rangle \tag{S15}$$

then, we recover the Eq. S10,

$$S(\omega_s, T) = \mathrm{Im} \int dt e^{i\omega_s(t-T)} \mathcal{E}_B^*(\omega_s) \mathcal{E}_N(t-T) \langle \boldsymbol{\sigma}(\boldsymbol{q}, t) \rangle \tag{S16}$$

showing that, in the minimal coupling, the transition polarizability in Eq. S10 is simply substituted by the transition charge densities. To get the TRUECARS signal, we computed effective polarizability value from transition charge density at 2450 eV. For example, the TRUECARS signal along $\boldsymbol{z}$ axis was calculated from the transition polarizability $\boldsymbol{\alpha}_{\mathrm{eff}}(\boldsymbol{q}) = \boldsymbol{\sigma}(\boldsymbol{q})$ at $\boldsymbol{q}_x = 0, \boldsymbol{q}_y = 0$, and $\boldsymbol{q}_z = |k_z| = \omega_s/c$ for the total of 128×128 nuclear coordinates, where ω_s is the probe carrier frequency of 90.036 *a.u.* and c is the speed of the light, 137.036 *a.u.*. By the same argument, TRUECARS signals along $\boldsymbol{x}$, and $\boldsymbol{y}$ axes were computed and shown in Figure. S4.

2.2 Off-Resonant Diffraction Signal

We follow the derivation of off-resonant time-resolved X-ray diffraction (TRXD) in refs [18][19]. An incident photon is scattered from the molecular charge density $\boldsymbol{\sigma}(\boldsymbol{q})$, where $\boldsymbol{\sigma}(\boldsymbol{q})$ is the Fourier transform of the real-space charge density $\boldsymbol{\sigma}(\boldsymbol{r})$. The scattering vector $\boldsymbol{q} = \boldsymbol{k}_s - \boldsymbol{k}_p$ represents the momentum transfer between incident ($\boldsymbol{k}_p$) and scattered ($\boldsymbol{k}_s$) photon. The molecular charge

density $\sigma(\boldsymbol{q})$ is a single-body electron operator which parametrically depends on nuclear coordinate $\boldsymbol{R}$, i.e., $\sigma(\boldsymbol{q}, \boldsymbol{R})$. The single-molecule TRXD signal [18][19] of a sample with N noninteracting molecule is expressed by

$$S_1(\boldsymbol{q}, T) \propto N \int dt |\mathcal{E}_X(t-T)|^2 \tilde{S}_1(\boldsymbol{q}, t) \tag{S17}$$

with the time delay T, X-ray probe pulse envelope $\mathcal{E}_X(t-T)$ centered at time T, and the time-dependent molecular response $\tilde{S}_1(\boldsymbol{q}, t)$. Using two electronic states (dark first excited state S_1 and the bright second excited state S_2), $\tilde{S}_1(\boldsymbol{q}, t)$ reads

$$\begin{aligned}
&\tilde{S}_1(\boldsymbol{q}, t) \\
&= \rho_{S_1S_1}(t) \langle \chi_{S_1}(t) | \sigma^\dagger_{S_1S_1} \sigma_{S_1S_1} | \chi_{S_1}(t) \rangle && (i) \\
&+ \rho_{S_2S_2}(t) \langle \chi_{S_2}(t) | \sigma^\dagger_{S_2S_2} \sigma_{S_2S_2} | \chi_{S_2}(t) \rangle && (ii) \\
&+ \rho_{S_1S_1}(t) \langle \chi_{S_1}(t) | \sigma^\dagger_{S_1S_2} \sigma_{S_2S_1} | \chi_{S_1}(t) \rangle && (iii) \\
&+ \rho_{S_2S_2}(t) \langle \chi_{S_2}(t) | \sigma^\dagger_{S_2S_1} \sigma_{S_1S_2} | \chi_{S_2}(t) \rangle && (iv) \\
&+ 2\mathrm{Re}[\rho_{S_2S_1}(t) \langle \chi_{S_2}(t) | \sigma^\dagger_{S_2S_2} \sigma_{S_2S_1} | \chi_{S_1}(t) \rangle + \rho_{S_2S_1}(t) \langle \chi_{S_2}(t) | \sigma^\dagger_{S_2S_1} \sigma_{S_1S_1} | \chi_{S_1}(t) \rangle] && (v)
\end{aligned} \tag{S18}$$

where each term corresponds to a particular loop diagram in Figure. S6. Here we write $\sigma(\boldsymbol{q}, \boldsymbol{R}) = \sigma$ for brevity. $\rho_{s_1s_1}$ and $\rho_{s_2s_2}$ are the electronic state populations, $\rho_{s_1s_2}$ is the coherence magnitude. Hence, the first (i) and the second (ii) term represent elastic scattering from the first and the second excited state, respectively. The third (iii) and fourth (iv) term describe inelastic scattering from both states. The last term (v) represents the mixed elastic/inelastic scattering from vibronic coherence. Note that our nuclear wavepacket does not decay to the ground state while it is absorbed at the S_1 minimum, hence we neglect the contribution from the ground state and consider only the contribution from S_1 and S_2 states.

3 Loop Diagram Rules

The loop diagram of the TRUECARS signal is shown in Scheme 1b in the main manuscript. The Diagram rules are as follows:

- Time runs along the loop clockwise from bottom left to bottom right.
- Each field interaction is represented by an arrow, which either points to the right (photon annihilation and excitation of the molecule) or to the left (photon creation and de-excitation of the molecule).
- Free evolution periods on the left branch indicate forward propagation in real time, and on the right branch to backward propagation respectively.
- The last field interaction (in this case, $\mathbf{k}_s$) is the detected photon mode. In addition, the gray bar represents the period of free evolution.

4 Result and Discussion

Prior to choosing the CASPT2 variant, we performed a detailed benchmarking of several CASPT2 flavors, namely SS-, MS- and XMS-CASPT2 [20]. For all methods we found comparable absorption and emission wavelengths, as well as similar reorganization energy in the S_2 and S_1 states. Among them, SS-CASPT2 with four extra-valence orbitals, compared to our simulation (full π active space (12/9)), reproduce better spectral line shapes in all three thiouracils (2-, 4-, and 2,4-). However, due to the extensive number of grids points required to build the reactive surfaces, we relied on a smaller full π active space.

To further extend our discussion, we optimized the critical points (the S_1 and S_2 minima and the CoIn) at each level (Table S1). The main discrepancy was observed in the CoIn region where the barrier to the CoIn increases in the sequence SS-CASPT2 $<$ XMS-CASPT2 $<$ MS-CASPT2. In fact, applying XMS-CASPT2 and MS-CASPT2 on top of the SS-CASPT2 CoIn leads to a S_2/S_1 splitting of 0.2 eV and 0.4 eV, respectively. As a consequence, the search for a "true" CoIn at the XMS- and MS-CASPT2 level distorts the molecule more pronouncedly which increases the CoIn energy and consequently, the barrier. In fact, the MS-CASPT2 lies well above the S_2 state at the FC point and remains unreachable.

MS-CASPT2 is known to overestimate the values of the off-diagonal couplings of the MS-CASPT2 Hamiltonian which leads to the observed pronounced splitting of 0.4 eV which leads to discontinuities on the PES. This over-splitting can be corrected by increasing the active space size in order to better describe the dynamic correlation already at the CASSCF level. XMS-CASPT2 resolves some of the issues of MS-CASPT2 (most notably providing smooth surfaces around the CoIn as it is invariant with respect to under unitary transformation of the WF). As a consequence, we observe a splitting of only 0.2 eV. The sensitivity of the couplings with respect to the active space size is still an issue though. Moreover, the use of an averaged zeroth order Fock operator (as the case with XMS) in the case of states of different character ($\pi\pi^*$ and $n\pi^*$) does not necessarily provide a better description with respect to the state-specific Fock operator. For this reason and due to the splitting of 0.2 and 0.4 eV observed at the XMS- and MS-CAPT2 level, we opted for SS-CASPT2.

Three-dimensional diffraction pattern and the projected diffraction signal integrating over $\boldsymbol{q}_x$, $\boldsymbol{q}_y$, or $\boldsymbol{q}_z$ are presented in Figure. S7 and S8, respectively. The total signals are dissected into the different contribution as labeled in Eq. 4. The dominant term is elastic scattering from population state: term (i) (excited state $\rho_{S_1S_1}$) and term (ii) (excited state $\rho_{S_2S_2}$) while the former being weaker than the latter one since $\rho_{S_2S_2}$ is larger than $\rho_{S_1S_1}$. The inelastic scattering terms (iii)/(iv) are 2026/2127 times weaker than their elastic counterpart when comparing their maximal intensity. The S_1 population term (i) and (iii) first appear at 20 fs and repeat its (dis)appearance as the nuclear WP oscillate between the FC and the CoIn. Another S_2 population term (ii) and (iv) are nonvanishing at the beginning, become intensified till 25 fs and start to vanish as the population decays. By the same argument, the coherence contribution (v) is 2118 times weaker than the maximal intensity of the total signal showing similar strength to the inelastic terms. It first shows up at 20 fs when S_2 WP passes by area with finite NAC. The coherence term exhibits both positive (red) and negative (blue) contributions showing the phase oscillation when comparing at 30, 50, and 61 fs.

The ratio of the each scattering contribution to the total signal is shown in Figure. S10. The ratio becomes finite above 4 $\AA^{-1}$ for coherence contribution (v), and above 6 $\AA^{-1}$ for inelastic contribu-

tions (iii and iv). The ratio for coherence term goes up to 0.014 at 50 fs and 14 $\AA^{-1}$ compared to the total signal. The total number of electrons for 4TU (66 electrons) is smaller than that of azobenzene (96 electrons), hence the ratios of terms (iii) to (v) against the total signal are somewhat larger than those of azobenzene [21]. The terms (iii) to (v) which involve transition charge density $\sigma_{S_2S_1}$ are more localized in the real-space thus being more spread in $\boldsymbol{q}$ space.

5 References

[1] Ignacio Fdez. Galván et al. "OpenMolcas: From Source Code to Insight". In: *Journal of Chemical Theory and Computation* 15.11 (2019). PMID: 31509407, pp. 5925–5964. DOI: 10.1021/acs.jctc.9b00532. eprint: https://doi.org/10.1021/acs.jctc.9b00532. URL: https://doi.org/10.1021/acs.jctc.9b00532.

[2] James Finley et al. "The multi-state CASPT2 method". In: *Chemical Physics Letters* 288.2 (1998), pp. 299–306. ISSN: 0009-2614. DOI: https://doi.org/10.1016/S0009-2614(98)00252-8. URL: https://www.sciencedirect.com/science/article/pii/S0009261498002528.

[3] Per-Olof Widmark, Per-Åke Malmqvist, and Björn O. Roos. "Density matrix averaged atomic natural orbital (ANO) basis sets for correlated molecular wave functions". In: *Theoretica chimica acta* 77.5 (Sept. 1990), pp. 291–306. ISSN: 1432-2234. DOI: 10.1007/BF01120130. URL: https://doi.org/10.1007/BF01120130.

[4] Oliver Weingart et al. "COBRAMM 2.0 — A software interface for tailoring molecular electronic structure calculations and running nanoscale (QM/MM) simulations". In: *Journal of Molecular Modeling* 24.9 (Sept. 2018), p. 271. ISSN: 0948-5023. DOI: 10.1007/s00894-018-3769-6. URL: https://doi.org/10.1007/s00894-018-3769-6.

[5] Rocío Borrego-Varillas et al. "Observation of the Sub-100 Femtosecond Population of a Dark State in a Thiobase Mediating Intersystem Crossing". In: *Journal of the American Chemical Society* 140.47 (2018), pp. 16087–16093. DOI: 10.1021/jacs.8b07057. eprint: https://doi.org/10.1021/jacs.8b07057. URL: https://doi.org/10.1021/jacs.8b07057.

[6] Danielle Cristina Teles-Ferreira et al. "A Unified Experimental/Theoretical Description of the Ultrafast Photophysics of Single and Double Thionated Uracils". In: *Chemistry – A European Journal* 26.1 (2020), pp. 336–343. DOI: https://doi.org/10.1002/chem.201904541. eprint: https://chemistry-europe.onlinelibrary.wiley.com/doi/pdf/10.1002/chem.201904541. URL: https://chemistry-europe.onlinelibrary.wiley.com/doi/abs/10.1002/chem.201904541.

[7] Artur Nenov et al. "Linear absorption spectra of solvated thiouracils resolved at the hybrid RASPT2/MM level". In: *Chemical Physics* 515 (2018). Ultrafast Photoinduced Processes in Polyatomic Molecules:Electronic Structure, Dynamics and Spectroscopy (Dedicated to Wolfgang Domcke on the occasion of his 70th birthday), pp. 643–653. ISSN: 0301-0104. DOI: https://doi.org/10.1016/j.chemphys.2018.07.025. URL: https://www.sciencedirect.com/science/article/pii/S0301010418303331.

[8] Daniel Keefer et al. "Controlling Photorelaxation in Uracil with Shaped Laser Pulses: A Theoretical Assessment". In: *Journal of the American Chemical Society* 139.14 (2017). PMID: 28187684, pp. 5061–5066. DOI: 10.1021/jacs.6b12033. eprint: https://doi.org/10.1021/jacs.6b12033. URL: https://doi.org/10.1021/jacs.6b12033.

[9] Sebastian Reiter, Daniel Keefer, and Regina de Vivie-Riedle. "Exact Quantum Dynamics (Wave Packets) in Reduced Dimensionality". In: *Quantum Chemistry and Dynamics of Excited States*. John Wiley Sons, Ltd, 2020. Chap. 11, pp. 355–381. ISBN: 9781119417774. DOI: https://doi.org/10.1002/9781119417774.ch11. eprint: https://onlinelibrary.wiley.com/doi/pdf/10.1002/9781119417774.ch11. URL: https://onlinelibrary.wiley.com/doi/abs/10.1002/9781119417774.ch11.

[10] H. Tal-Ezer and R. Kosloff. "An accurate and efficient scheme for propagating the time dependent Schrödinger equation". In: *The Journal of Chemical Physics* 81.9 (1984), pp. 3967–3971. DOI: 10.1063/1.448136. eprint: https://doi.org/10.1063/1.448136. URL: https://doi.org/10.1063/1.448136.

[11] Hans-Dieter Meyer, Fabien Gatti, and Graham A. Worth. "Basic MCTDH Theory". In: *Multidimensional Quantum Dynamics*. John Wiley Sons, Ltd, 2009. Chap. 3, pp. 17–30. ISBN: 9783527627400. DOI: https://doi.org/10.1002/9783527627400.ch3. eprint: https://onlinelibrary.wiley.com/doi/pdf/10.1002/9783527627400.ch3. URL: https://onlinelibrary.wiley.com/doi/abs/10.1002/9783527627400.ch3.

[12] M. Ben-Nun, Jason Quenneville, and Todd J. Martínez. "Ab Initio Multiple Spawning: Photochemistry from First Principles Quantum Molecular Dynamics". In: *The Journal of Physical Chemistry A* 104.22 (2000), pp. 5161–5175. DOI: 10.1021/jp994174i. eprint: https://doi.org/10.1021/jp994174i. URL: https://doi.org/10.1021/jp994174i.

[13] Sebastian Thallmair, Matthias K. Roos, and Regina de Vivie-Riedle. "Design of specially adapted reactive coordinates to economically compute potential and kinetic energy operators including geometry relaxation". In: *The Journal of Chemical Physics* 144.23 (2016), p. 234104. DOI: 10.1063/1.4953667. eprint: https://doi.org/10.1063/1.4953667. URL: https://doi.org/10.1063/1.4953667.

[14] Matthias Ruckenbauer et al. "Photoelectron spectra of 2-thiouracil, 4-thiouracil, and 2,4-dithiouracil". In: *The Journal of Chemical Physics* 144.7 (2016), p. 074303. DOI: 10.1063/1.4941948. eprint: https://doi.org/10.1063/1.4941948. URL: https://doi.org/10.1063/1.4941948.

[15] Markus Kowalewski et al. "Catching Conical Intersections in the Act: Monitoring Transient Electronic Coherences by Attosecond Stimulated X-Ray Raman Signals". In: *Phys. Rev. Lett.* 115 (19 Nov. 2015), p. 193003. DOI: 10.1103/PhysRevLett.115.193003. URL: https://link.aps.org/doi/10.1103/PhysRevLett.115.193003.

[16] Jérémy R. Rouxel, Markus Kowalewski, and Shaul Mukamel. "Current vs Charge Density Contributions to Nonlinear X-ray Spectroscopy". In: *Journal of Chemical Theory and Computation* 12.8 (2016). PMID: 27347786, pp. 3959–3968. DOI: 10.1021/acs.jctc.6b00279. eprint: https://doi.org/10.1021/acs.jctc.6b00279. URL: https://doi.org/10.1021/acs.jctc.6b00279.

[17] Vladimir Y. Chernyak, Prasoon Saurabh, and Shaul Mukamel. "Non-linear non-local molecular electrodynamics with nano-optical fields". In: *The Journal of Chemical Physics* 143.16 (2015), p. 164107. DOI: 10.1063/1.4934231. eprint: https://doi.org/10.1063/1.4934231. URL: https://doi.org/10.1063/1.4934231.

[18] Kochise Bennett et al. “Monitoring molecular nonadiabatic dynamics with femtosecond X-ray diffraction”. In: *Proceedings of the National Academy of Sciences* 115.26 (2018), pp. 6538–6547. ISSN: 0027-8424. DOI: 10.1073/pnas.1805335115. eprint: https://www.pnas.org/content/115/26/6538.full.pdf. URL: https://www.pnas.org/content/115/26/6538.

[19] Jérémy R. Rouxel, Daniel Keefer, and Shaul Mukamel. “Signatures of electronic and nuclear coherences in ultrafast molecular x-ray and electron diffraction”. In: *Structural Dynamics* 8.1 (2021), p. 014101. DOI: 10.1063/4.0000043. eprint: https://doi.org/10.1063/4.0000043. URL: https://doi.org/10.1063/4.0000043.

[20] Artur Nenov et al. “Linear absorption spectra of solvated thiouracils resolved at the hybrid RASPT2/MM level”. In: *Chemical Physics* 515 (2018). Ultrafast Photoinduced Processes in Polyatomic Molecules:Electronic Structure, Dynamics and Spectroscopy (Dedicated to Wolfgang Domcke on the occasion of his 70th birthday), pp. 643–653. ISSN: 0301-0104. DOI: https://doi.org/10.1016/j.chemphys.2018.07.025. URL: https://www.sciencedirect.com/science/article/pii/S0301010418303331.

[21] Daniel Keefer et al. “Imaging conical intersection dynamics during azobenzene photoisomerization by ultrafast X-ray diffraction”. In: *Proceedings of the National Academy of Sciences* 118.3 (2021), e2022037118. ISSN: 0027-8424. DOI: 10.1073/pnas.2022037118. eprint: https://www.pnas.org/content/118/3/e2022037118.full.pdf. URL: https://www.pnas.org/content/118/3/e2022037118.

6 Supplementary Figures

Table S 1: Comparison of the electronic structure of 4-thiouracil at several critical points - ground and two lowest excited state minima, and S_2/S_1 conical intersection (CoIn) denoted as S_0 min, S_1 min (nπ^*), S_2 min ($\pi\pi^*$), and S_2/S_1 CoIn, optimized with different flavors of the CASPT2 protocol - single state (SS-PT2), extended multi state (XMS-PT2), and multi state (MS) on top of a SA-3-CASSCF(12,9) calculation. All data are shown in eV unit. XMS-PT2 and MS-PT2 calculations on top of the CoIn optimized at the SS-PT2 level reveal a progressively increasing splitting (0.2 eV at XMS-PT2, 0.4 eV at MS-PT2).

SS-PT2	S_0 min	S_2 min	S_2/S_1 CoIn	S_1 min
S0	0.00	0.88	1.92	0.26
S1(nπ^*)	2.66	2.65	3.42	2.40
S2($\pi\pi^*$)	3.84	3.11	3.41	3.34
XMS-PT2	S_0 min	S_2 min	S_2/S_1 CoIn	S_1 min
S0	0.00	0.57	1.67	0.23
S1(nπ^*)	2.82	2.69	3.54	2.55
S2($\pi\pi^*$)	3.92	3.30	3.75	3.46
MS-PT2	S_0 min	S_2 min	S_2/S_1 CoIn	S_1 min
S0	0.00	0.51	1.61	0.22
S1(nπ^*)	2.77	2.64	3.52	2.50
S2($\pi\pi^*$)	4.04	3.43	3.93	3.59

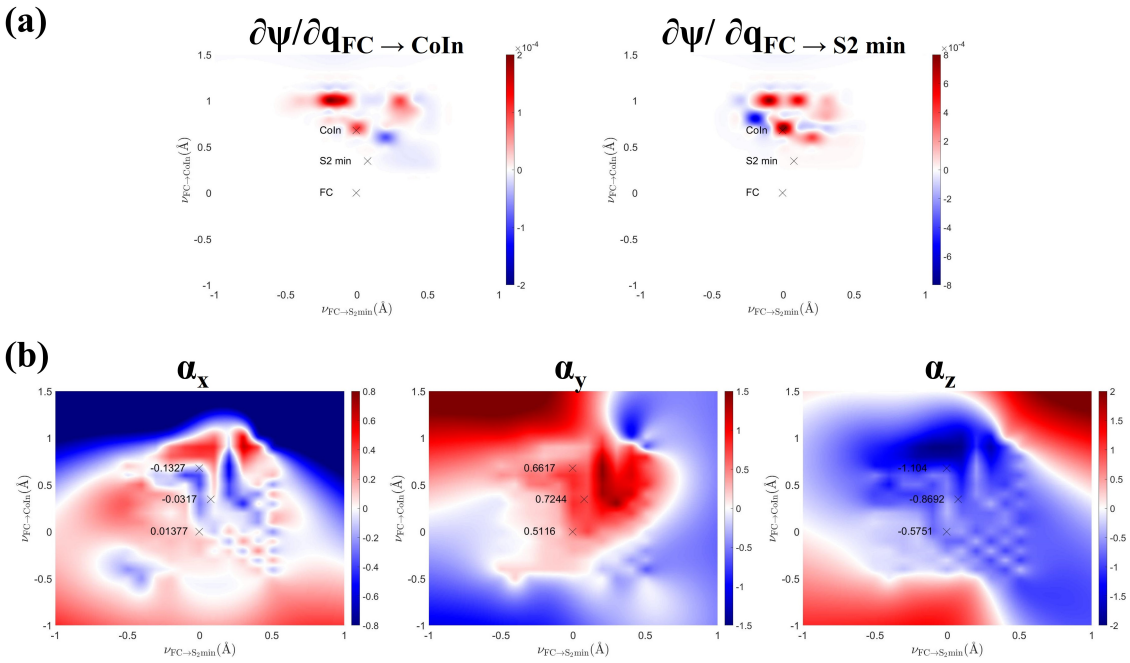

Figure. S 1: (a) Nonadiabatic couplings versus the two nuclear coordinates of the molecules. The location of the FC, CoIn, and S_2 min are marked with X. (b) $S_2 - S_1$ transition probabailities at 2450 eV. The transition polarizability values are given for the location of the FC, CoIn, and S_2 min (marked with X).

Figure. S 2: The complete nuclear wavepacket dynamics movie on the S_2 (left) and the S_1 (right) potential energy surface. S_2 wavepacket (grey contours), S_1 wavepacket (pink contour). See the attached video.

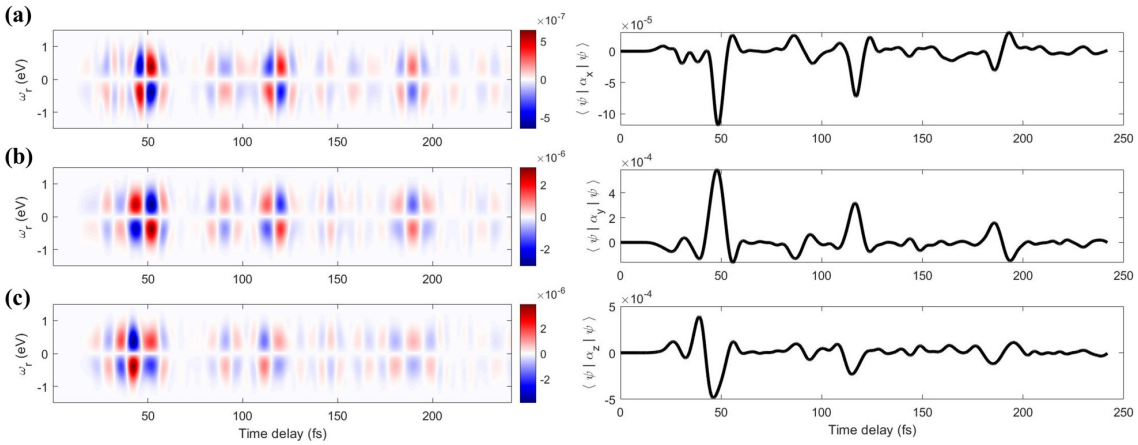

Figure. S 3: Comparison of molecular orientation in the TRUECARS signal along a) $\boldsymbol{x}$ ($\boldsymbol{\alpha}_x$), (b) $\boldsymbol{y}$ ($\boldsymbol{\alpha}_y$), and (c) $\boldsymbol{z}$ ($\boldsymbol{\alpha}_z$) axis. The $\boldsymbol{y}$ and $\boldsymbol{z}$ component exhibits stronger signal than the $\boldsymbol{x}$ component. The left figures show the TRUECARS signal and the right figrues show the expectation value of the polarizability operator for each direction

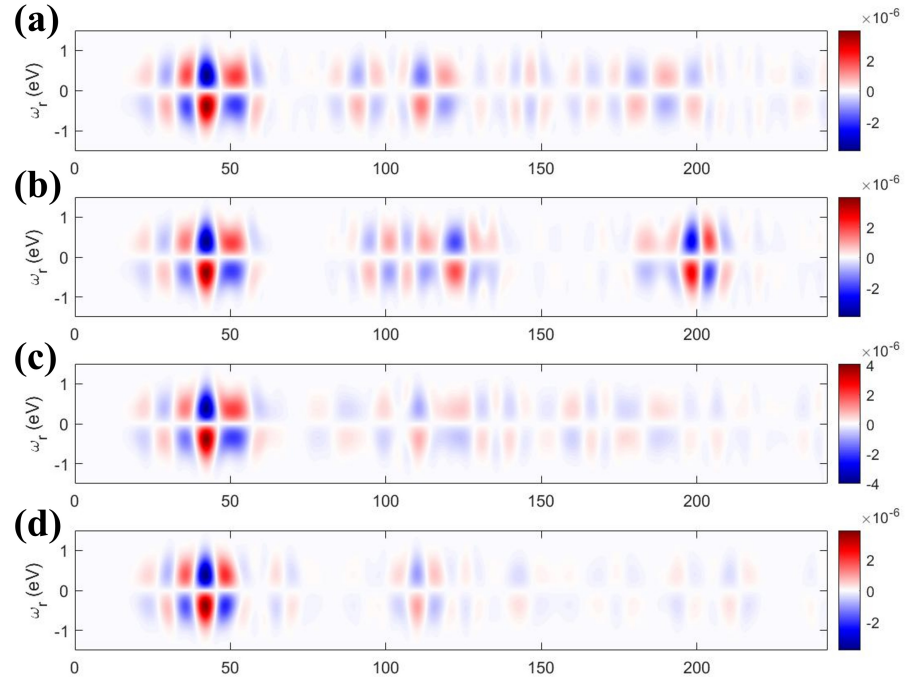

Figure. S 4: The TRUECARS signal along z axis at the different placement of Gobblers. $\nu_{\mathrm{FC}\rightarrow\mathrm{CoIn}}$ = (a) -0.1 (near S_1 min), (b) -1.0 (far below S_1 min), (c) 0.55, and (d) 1.0.

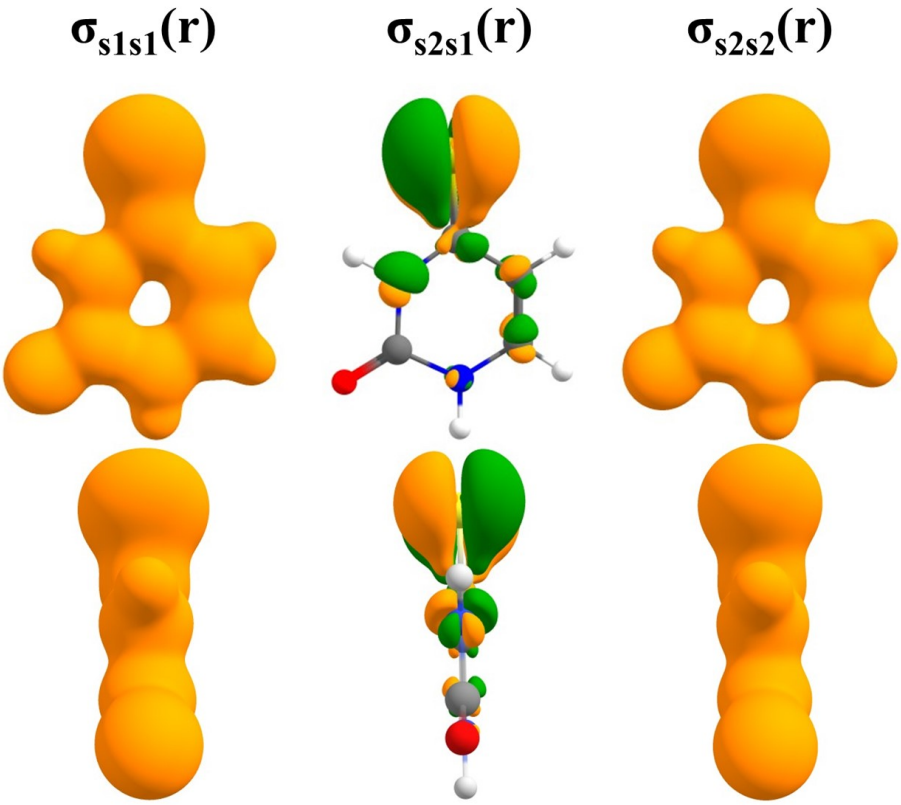

Figure. S 5: Real-space charge densities of 4TU at the conical intersection geometry (isovalue 0.025 for $\sigma_{S_1S_1}$ and $\sigma_{S_2S_2}$, 0.0025 for $\sigma_{S_2S_1}$)

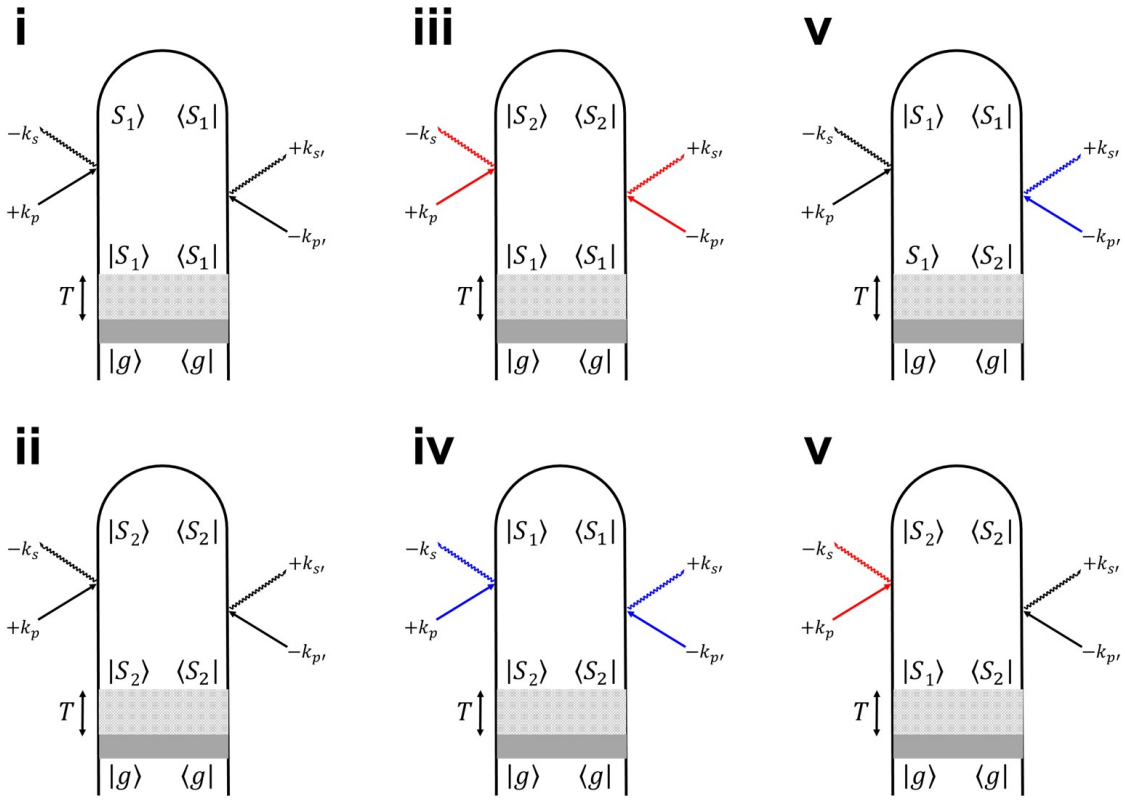

Figure. S 6: Loop diagrams for single-molecule X-ray scattering process. The shaded area represents an excitation that prepares the system in $|S_2\rangle$ state. The checkered box represents a field-free nonadiabatic dynamics during time delay T. We denote modes of the X-ray probe pulse with p and p', whereas s and s' represent relevant scattering modes. Elastic scattering process are denoted by black field arrows. Inelastic processes are denoted by red (stokes) or blue (anti-stoke) arrows.

Figure. S 7: Time-resolved three-dimensional diffraction pattern. Each term is labeled according to Eq. 4. The red (blue) isosurface in term (vi) corresponds to gain(loss) temporal phase-oscillations. See the attached video.

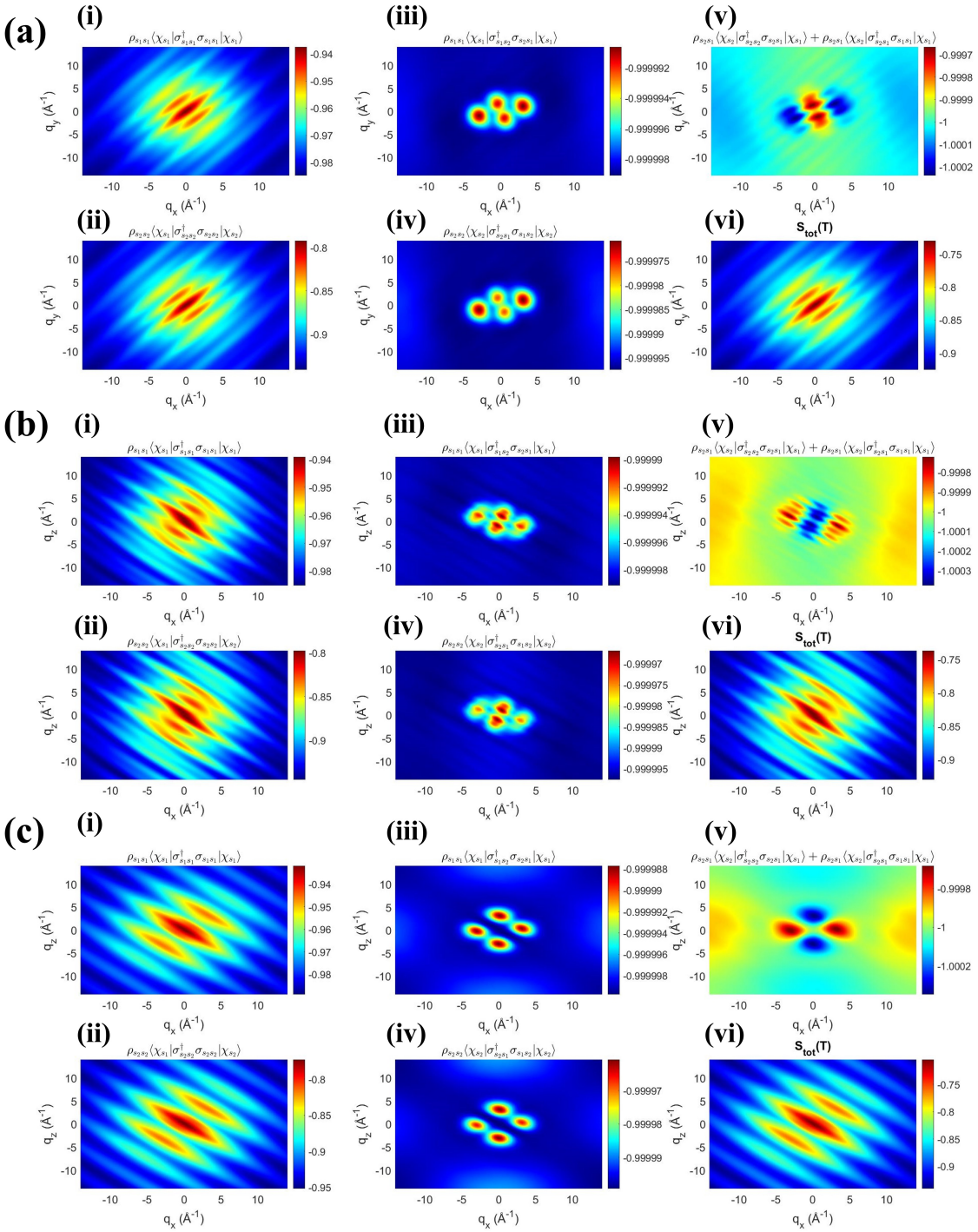

Figure. S 8: Normalized two-dimensional diffraction patterns in the (a) $\boldsymbol{q}_{xy}$, (b) $\boldsymbol{q}_{xz}$, and (c) $\boldsymbol{q}_{yz}$ planes, after integrating over the respective other direction at 45 fs. Each term is labeled according to Eq. 4.

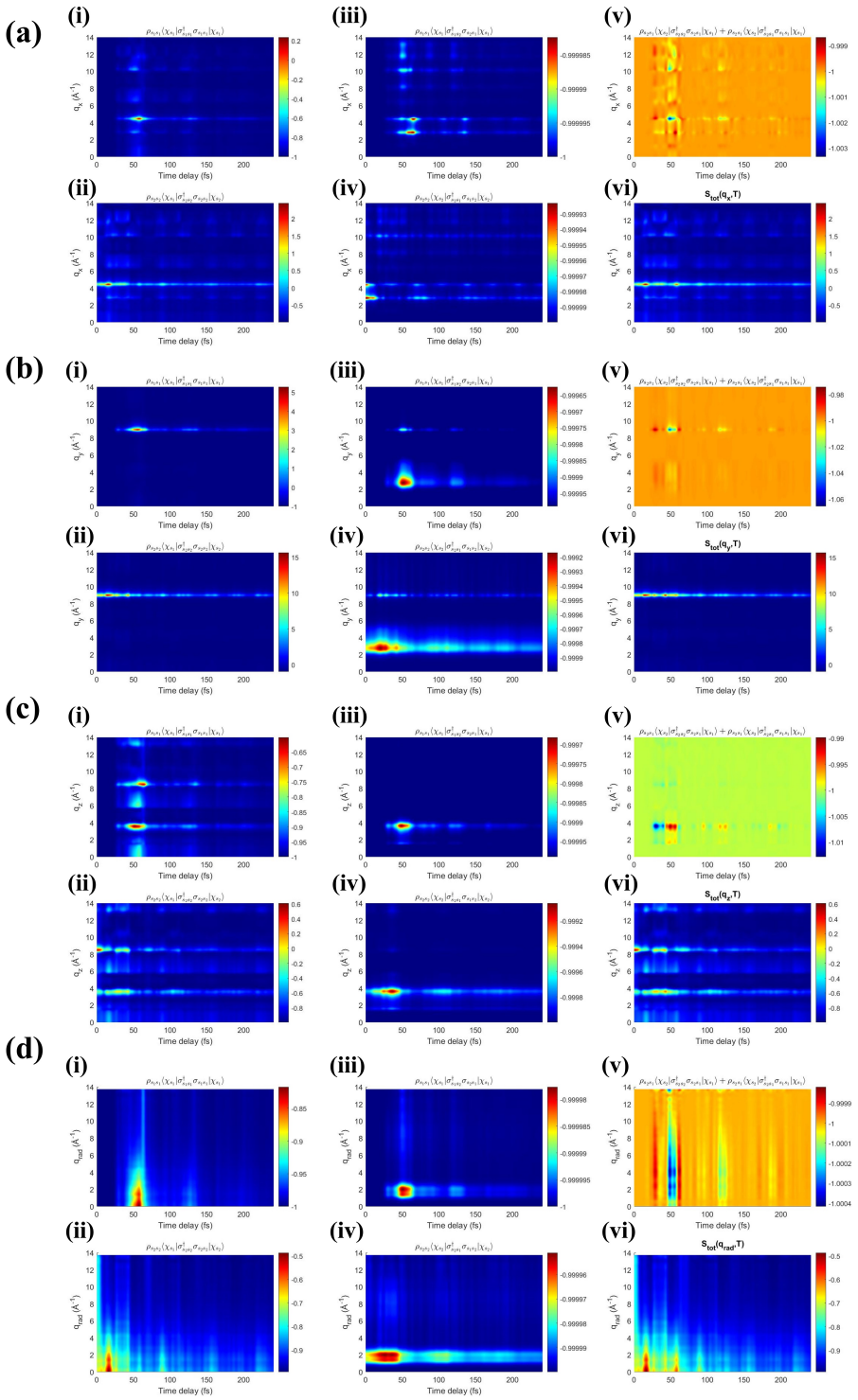

Figure. S 9: Normalized time-resolved diffraction signal $S(\boldsymbol{q}, T)$ along (a)$\boldsymbol{q}_x$, (b)$\boldsymbol{q}_y$, (c)$\boldsymbol{q}_z$, and (d)$\boldsymbol{q}_{rad}$ directions.

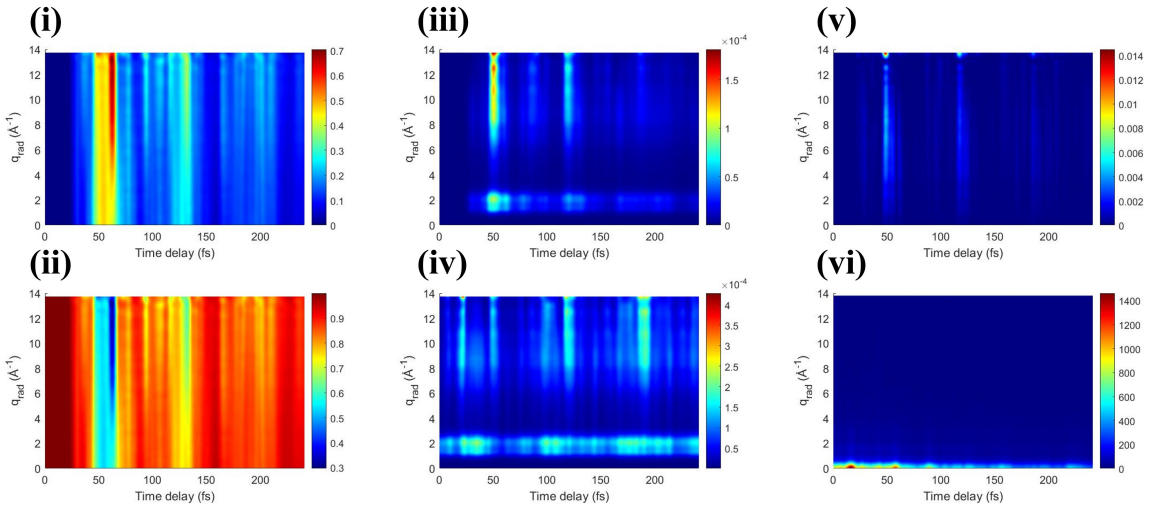

Figure. S 10: (i)-(v) Ratio of the strength of each contribution (labeled according to Eq. 4) in Figure. S9d vs in the total signal (vi).